University of Tennessee, Knoxville

TRACE: Tennessee Research and Creative Exchange

Masters Theses

Graduate School

12-1998

X-ray fluorescence microtom[o]graphy of trace elements in a SiC nuclear fuel shell

Masoud Naghedolfeizi

Follow this and additional works at: https://trace.tennessee.edu/utk_gradthes

Recommended Citation

Naghedolfeizi, Masoud, "X-ray fluorescence microtom[o]graphy of trace elements in a SiC nuclear fuel shell. " Master's Thesis, University of Tennessee, 1998.
https://trace.tennessee.edu/utk_gradthes/10325

This Thesis is brought to you for free and open access by the Graduate School at TRACE: Tennessee Research and Creative Exchange. It has been accepted for inclusion in Masters Theses by an authorized administrator of TRACE: Tennessee Research and Creative Exchange. For more information, please contact trace@utk.edu.

To the Graduate Council:

I am submitting herewith a thesis written by Masoud Naghedolfeizi entitled "X-ray fluorescence microtom[o]graphy of trace elements in a SiC nuclear fuel shell." I have examined the final electronic copy of this thesis for form and content and recommend that it be accepted in partial fulfillment of the requirements for the degree of Master of Science, with a major in Metallurgical Engineering.

Carl J. McHargue, Major Professor

We have read this thesis and recommend its acceptance:

Joseph E. Spruiell, Thomas T. Meek

Accepted for the Council:
Carolyn R. Hodges

Vice Provost and Dean of the Graduate School

(Original signatures are on file with official student records.)

To the Graduate Council:

I am submitting herewith a thesis written by Masoud Naghedolfeizi entitled "X-ray Fluorescence Microtomography Study of Trace Elements in a SiC Nuclear Fuel Shell." I have examined the final copy of this thesis for form and content and recommend that it be accepted in partial fulfillment of the requirements for the degree of Master of Science, with a major in Metallurgical Engineering.

Carl J. McHargue, Major Professor

We have read this thesis
and recommend its acceptance:

Accepted for the Council:

Associate Vice Chancellor
and Dean of the Graduate School

X-RAY FLUORESCENCE MICROTOMGRAPHY OF TRACE ELEMENTS IN A SiC NUCLEAR FUEL SHELL

A Thesis
Presented for the
Master of Science
Degree
The University of Tennessee, Knoxville

Masoud Naghedolfeizi

December 1998

ACKNOWLEDGMENTS

The author would like to take the opportunity to express sincere appreciation and gratitude to his major professor and committee chairman, Dr. Carl J. McHargue, for his guidance and encouragement during the course of this research work. Professor McHargue has diligently served in his role as chairman, but much more than that he has served as a role model for his graduate students through the years and as an outstanding scientist in the field of materials sciences. His efforts in providing the author the opportunity to meet and work with Dr. Gene E. Ice, the group leader of x-ray research and development of Oak Ridge National Laboratory (ORNL), are gratefully acknowledged.

Special appreciation is expressed to Dr. Gene E. Ice whose encouragement, patience, and untiring devotion and enthusiasm to the field of x-ray science have been an inspiration to the author. Dr. Ice has provided the interest, invaluable technical assistance, direction, advice, and warm support so necessary and vital during the course of this research endeavor. His financial supports of both the research work and the author are gratefully appreciated. The author feels fortunate that he has had the opportunity to work with such an outstanding scientist for almost two years.

The author wishes to express his appreciation to professor Joseph E. Spruiell, the department head, and Professor Thomas T. Meek for serving on his thesis committee and for their interest, comments and suggestions. Special thanks go to professor Spruiell for

introducing professor McHargue to me and for taking time from his busy schedule to attend in the thesis committee.

The author also wishes to express his appreciation to Dr. Cullie J. Sparks, Dr. Jin-Seok Chung, and Dr. Eliot D. Specht of ORNL for their useful comments, assistance, and many interesting scientific and social discussions. Thanks are due to the staff of the advanced photon source (APS) for providing experimental facilities and technical assistance.

The author is also grateful to Mrs. Sherry hempfling of ORNL and Mrs. Jewell Johnson of the University of Tennessee for their secretarial assistance and for providing a comfortable working environment.

This work was sponsored in part by the Laboratory Directed Research and Development Program of the ORNL and the Division of Materials Sciences, U.S. Dept. of Energy under contract with Lockheed Martin Energy Research Corporation.

ABSTRACT

The advent of third generation synchrotrons and the ongoing revolution in x-ray focusing optics have contributed to the development of x-ray probes with micron and submicron resolution. As a result , it is now possible to perform micro-structural analysis of materials with techniques previously not possible. In this thesis, x-ray fluorescence microtomography, a comparatively new technique, coupled with a synchrotron x-ray microprobe of micron resolution were used to study the trace element distributions in a SiC shell of an advanced nuclear fuel particle, known as TRISO. The TRISO fuel particles contain a small kernel of nuclear fuel encapsulated by alternating layers of C and a barrier layer of SiC. The SiC shell provides the primary barrier for radioactive elements in the kernel and metallic fission products. The performance of this barrier under adverse conditions is key to containment.

The tomographic measurements were made with an ~1x3 μm^2 x-ray probe on beamline 2-ID at the Advanced Photon Source (APS). The distribution of trace elements in the SiC shell was reconstructed after correcting the data for artifacts arising from absorption and scattering off the kapton tape used to encapsulate the sample. The tomographic reconstructions were carried out, both with and without absorption correction. The images obtained in both reconstruction cases show that the SiC shell is ~38 μm thick, and the observed trace elements are distributed in small <1 μm regions through the SiC shell. The results also indicates that most trace elements have localized distributions within the SiC shell. The trace elements can be attributed to radiation enhanced diffusion of elements in the kernel or to trace elements introduced during fabrication. The

investigation of the reconstructed images with absorption correction indicates that for low energy fluorescence lines the effect of SiC absorption is rather significant in estimating the concentration of trace elements.

The overall results of this research study verifies that X-ray fluorescence microtomography is an ideal tool for detecting high Z trace elements in a low Z matrix because it is a sensitive and penetrating nondestructive probe and because it provides a picture of the elemental distribution with micron spatial resolution. The advantages of x-ray fluorescence tomography for the non-destructive 3-D characterization of materials will continue to grow as x-ray source brilliance increases.

TABLE OF CONTENTS

CHAPTER		PAGE
1.	**INTRODUCTION**	**1**
	1.1 Background	1
	1.2 Statement of the Problem	4
	1.3 X-ray Fluorescence Microtomography	6
	1.4 Previous Studies and Sample Preparation	9
	1.5 Significance of the Research	9
	1.6 Organization of the Thesis	11
2.	**X-RAY MICROTOMOGRAPHY**	**13**
	2.1 Introduction	13
	2.2 X-ray Computerized Tomography	13
	2.3 Basic Instrumentation of X-ray Fluorescence Microtomography	16
	2.4 Mathematical Representation of Computed Tomography	20
	2.5 Image Reconstruction Algorithms	26
	2.5.1 Backprojection of Filtered Projection Algorithm	29
	2.6 Factors Influencing the Image Reconstruction Quality	36
	2.7 Qualitative Comparison between Elemental Sensitivity in Transmission Microtomography and Fluorescence Microtomography	37
3.	**FLUORESCENCE MICROTOMOGRAPHY EXPERIMENT**	**43**
	3.1 Experimental Setup	43
	3.2 X-ray Fluorescence Microtomography Experiment	46

4. RESULTS AND EXPERIMENTAL ANALYSIS 53

4.1 Preprocessing and Analysis of Projection Data 53

4.2 Image Reconstruction Procedure 58

4.3 Estimation of Elemental Concentration 60

4.4 Analyses of Tomographic Images 63

5. SUMMARY, CONCLUSIONS, AND RECOMMENDATIONS FOR FUTURE WORKS 72

5.1 Summary 72

5.2 Conclusions 74

5.3 Recommendations for Future Works 75

REFERENCES 77

APPENDICES 80

A. SYNCHROTRON RADIATION AND BEAMLINE 2-ID AT THE ADVANCED PHOTON SOURCE 81

A.1 Synchrotron Radiation 81
A.2 Beamline 2-ID at the Advanced Photon Source 83

B. NUMERICAL AND COMPUTER IMPLEMENTATION OF BACK PROJECTION OF FILTERED PROJECTION 87

C. LISTING OF COMPUTER PROGRAMS 94

VITA 110

LIST OF TABLES

TABLE **PAGE**

1.1 Selected isotopes and irradiation conditions for irradiated TRISO Particles [4] 10

2.1 Linear absorption coefficients below and above the K absorption edge for the monitored trace elements in SiC shell of the TRISO fuel ball 40

3.1 Measured regions of interest (ROIs) in the fuel ball spectrum 49

4.1 Linear absorption coefficients of SiC at measured ROI energies 61

LIST OF FIGURES

FIGURE **PAGE**

1.1 Trends in brilliance of x-ray sources over the last 100 years [3] 3

1.2 Schematic diagram of a typical TRISO fuel element 5

1.3 Schematic diagram of x-ray microfluorescence measurements 8

2.1 Schematic diagram of data collection in transmission tomography and fluorescence tomography 15

2.2 Schematic diagram of a typical experimental setup for fluorescence microtomography measurements 17

2.3 Changes in x-ray beam size over the last decade [15] 19

2.4 Decay of beam current (intensity) with time 21

2.5 Data collection in transmission tomography [21] 22

2.6 Data collection in fluorescence microtomography 24

2.7 Coordinate systems for image reconstruction in computerized tomography 27

2.8 Artifacts produced in image reconstruction of a central point using back-projection of filtered projection algorithm [21] 30

2.9 The coordinate system used for the back-projection of filtered projection [21] 32

2.10 Frequency characteristics of window functions and filter functions [19] 35

2.11 Attenuation of x-ray beam intensity in a transmission tomography 39

3.1 Schematic diagram of the experimental setup used to perform fluorescence microtomography experiments at beamline 2-ID of the APS 44

3.2 Time decay of photon intensity in the APS 2-ID beamline during the tomography experiment 47

3.3 Measured fluorescence spectrum from an unfocused beam on the SiC fuel ball shell 48

3.4 Measured fluorescence intensities of trace elements in a linescan experiment on TRISO fuel particle 51

4.1 Plots of tomographic data of the monitored regions-of-interests (ROIs) in a TRISO nuclear fuel ball 55

4.2 Reconstructed images of the spatial distribution of trace elements without absorption correction. The reconstructed elemental distributions are superimposed on the reconstructed shell from the elastic/Compton scattering 64

4.3 Reconstructed images of the spatial distribution of trace elements with absorption correction 67

A.1 Schematic diagram of the advanced photon source (APS) 82

A.2 Schematic diagram of beamline 2-ID at the advanced photon source (APS) [25]. 84

B.1 Analytical projection data for an ellipse with a uniform density [21] 90

C.1 Image reconstruction grid in a parallel-beam geometry [19] 95

CHAPTER 1

INTRODUCTION

1.1 Background

In recent years, there has been a growing need in various areas of science and technology to non-destructively examine the internal structure of advanced materials with high spatial resolution. Since many advanced materials depend on structures that are as small as 1 micron or even less, inspection probes on the order of micron or submicron sizes are required to characterize the relevant microstructural features. Conventional inspection techniques such as scanning tunneling microscopy or electron and optical microscopy can provide 3-D micron to submicron resolution only in a destructive manner [1-2]. These methods require serial sectioning and staining of the sample, which can alter (or even destroy) the original structural features. In some cases, even destructive methods may be impractical because of physical and /or environmental restrictions(e.g.; radioactive samples). Conventional x-ray based non-destructive methods such as transmissive radiography and laminographic imaging can achieve spatial resolutions on the order of hundreds of microns but new synchrotron based methods are required to approach the micron or submicron regime [1].

An extension of conventional tomography for nondestructive and noninvasive imaging, known as microtomography now exists which can provide high spatial resolution and

detailed imaging information about the internal structures of objects. Microtomography utilizes synchrotron x-rays, advanced focusing optics, and precision x-ray detectors to achieve micron size spatial resolution. Synchrotron radiation possesses unique characteristics which allow the measurement of internal structures with micron resolution. Synchrotron radiation is extremely intense and highly collimated. It covers a wide range of energy spectra from the infrared to 200 keV. In addition, it can provide a tunable monochromatic x-ray beam with minimum beam hardening effects [3]. For example, synchrotron x-ray sources can provide x-ray brilliance up to 14 orders of magnitude higher than from conventional laboratory or medical sources [3]. Figure 1.1 presents the trends in the x-ray brilliance over the last century. As can be seen in the figure, there has been significant progress in improving the x-ray brilliance since the advent of synchrotron technology. Presently, the Advanced Photon Source (APS) provides the greatest x-ray brilliance at $\sim 5\times10^{11}$ (photons/s/3eV/mrad^2/μm^2). Since the figure-of-merit for microfluorescence is brilliance [9], 12 to 14 orders of magnitude increase in the brilliance will allow for x-ray fluorescence microtomography with micron resolution. However, with laboratory and medical x-ray sources, insufficient x-ray brilliance limits the achievable spatial resolution to approximately one millimeter or slightly better [1-2].

Microtomography technology is currently gaining popularity as a result of its unique and attractive features. It has become more widely recognized as an alternative to

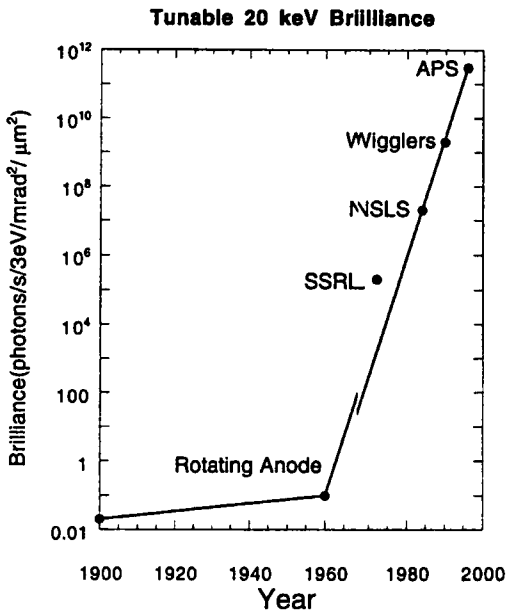

Figure 1.1: Trends in brilliance of x-ray sources over the last 100 years [3].

destructive testing for microstructural analysis of advanced materials since it allows repeated measurements on the same samples. Microtomography has found a wide range of applications in biological, medical, chemical, and materials sciences. From internal imaging of a bee's head to complex and heterogeneous microelectronic chips, this imaging technology has proven to have a major impact for both science and industry. With current and future advances in synchrotron technology and x-ray focusing optics, microtomography can help revolutionize the design and development of advanced materials.

This thesis takes advantage of an ongoing revolution in x-ray science to nondestructively measure trace chemical inhomogenities with near micron resolution. This work illustrates the unique advantages of x-ray microtomography for nondestructive trace element analysis. The ability to nondestructively measure trace element inhomogenities in 3-D will have a major impact on our understanding of advanced materials.

1.2 Statement of the Problem

The study of TRISO fuel particles presented a good opportunity to demonstrate the unique advantages of x-ray fluorescence microtomography on a complex material system. TRISO fuel particles, used in High-Temperature Gas Cooled Reactors (HTGR) are composite structures with a nuclear fuel kernel surrounded by alternating layers designed to contain fission products and compensate for radiation damage. As shown in Fig. 1.2, a typical fuel particle contains an inner kernel of nuclear fuel, a low density buffer layer of pyrocarbon, a dense layer of pyrocarbon coating, an interlayer of SiC and an outer dense

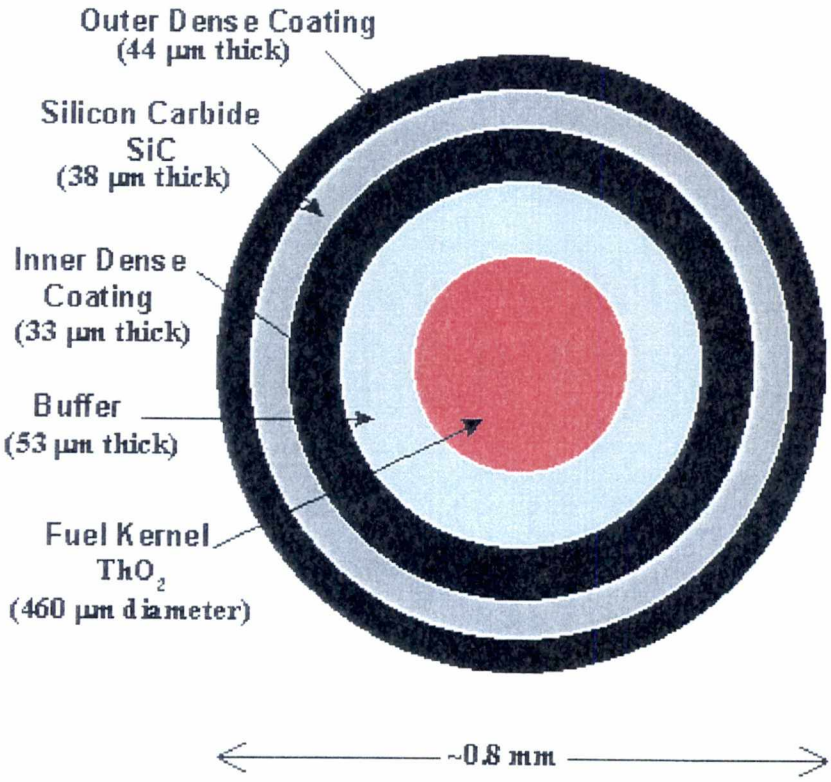

Figure 1.2: Schematic diagram of a typical TRISO fuel element.

layer of pyrocarbon. Depending on the type of reactor core design, the fuel kernel is chosen from UCO, UC_2, ThO_2, or UO_2. In addition, fuel kernel size, the thickness of the various layers, and the overall size of the TRISO fuel particle can vary with the type of fuel kernel [4]. TRISO coated fuel particles are compacted into fuel rods designed for passive containment of the radioactive isotopes. The SiC layer provides the primary barrier for both radioactive elements in the kernel and gaseous and metallic fission products. The effectiveness of this barrier layer under adverse conditions is critical to containment and has been the subject of previous studies [4,5].

The goal of this research study is to investigate and characterize the spatial distribution of trace elements in the SiC shell of a typical TRISO fuel particle after exposure to a fluence of ~ 10^{25} (neutrons/m^2). X-ray fluorescence microtomography is an ideal tool for this work because it is nondestructive, it is sensitive to heavy elements in a low Z matrix, and because it can provide a high resolution 3-D picture of the elemental distribution. The observed elemental distribution can be later correlated with flaws and defects in the SiC shell.

1.3 X-ray Fluorescence Microtomography

The advent of intense synchrotron radiation sources has improved the resolution of tomography into the micron regime. Although most tomographic measurements use transmission tomography methods [6-8], experiments as early as 1985 demonstrated the elemental sensitivity of fluorescence tomography to high Z trace elements in a low Z matrix [9]. These pioneering measurements of the Fe distribution in a honey bee (*Apis*

mellifera) found Fe concentrations at the surface and in the abdomen of the bee with a spatial resolution of ~150μm.

The experimental setup for an x-ray fluorescence tomography measurement is conceptually very simple (Fig. 1.3). The sample is placed on a stage which rotates and translates the sample. A detector is placed in the plane of the synchrotron storage ring and at 90° to the incident beam. This detector geometry allows efficient measurement of the characteristic fluorescence from the trace elements while minimizing the x-ray elastic and Compton scattering [10]. The elemental distribution in a slice through the sample can be reconstructed after translating the sample through the x-ray beam and rotating the sample at least 180° for every x position. Finer resolution is achieved by decreasing both the translation and rotational step size.

With new x-ray focusing optics and sources, μm^3 fluorescence microtomography is now practical. Fluorescence tomography however is very slow compared to transmission tomography because the number of volume elements (voxels) which can be resolved scales roughly with the number of data points collected. In contrast, transmission tomography measures the attenuation through all translation positions simultaneously and therefore has an ~ 10^6 faster collection time. Although transmission measurements are much faster, fluorescence measurements have better signal-to-noise for trace element detection [10]. Fluorescence tomography is therefore most appropriate for use on

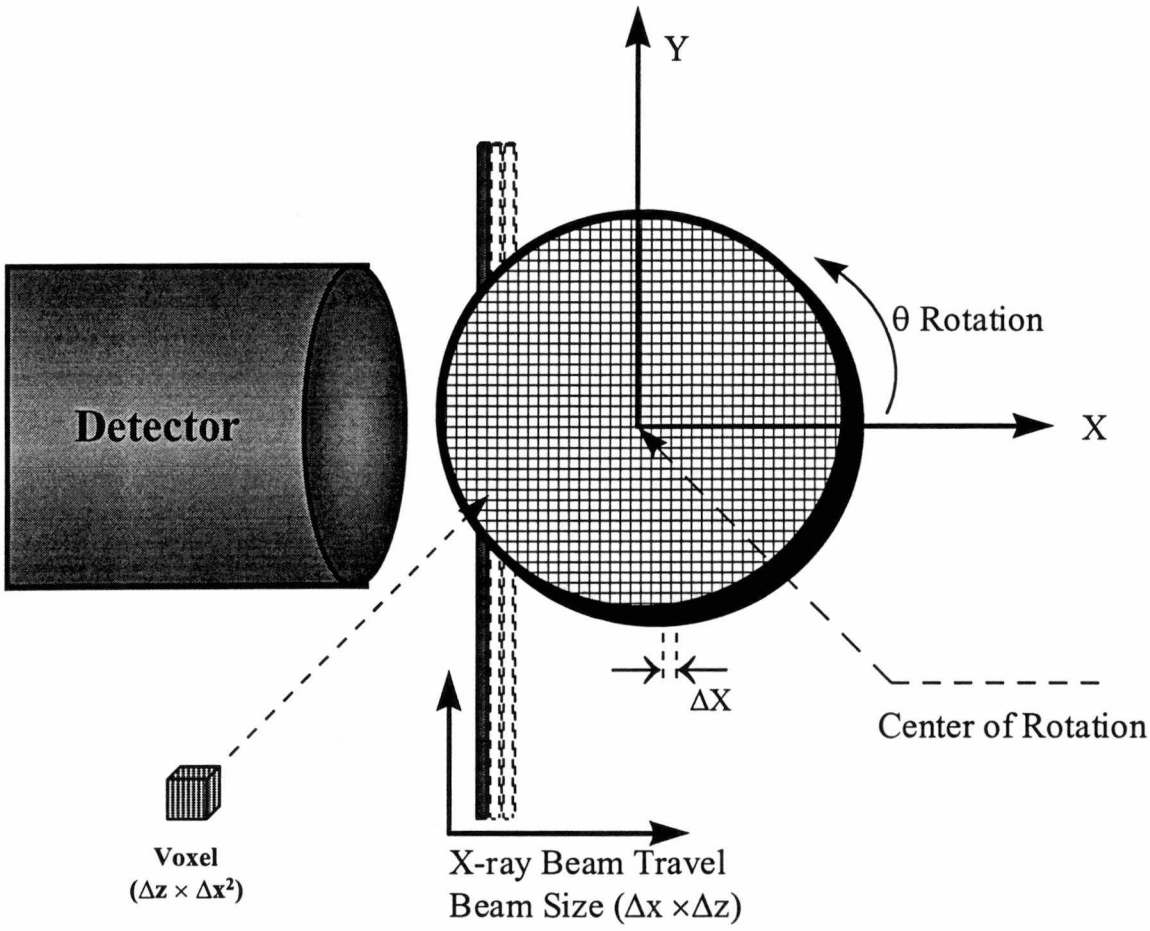

Figure 1.3: Schematic diagram of x-ray microfluorescence measurements.

materials where there is interest in the distribution of very low concentrations of trace elements which challenge the sensitivity of transmission tomography.

1.4 Previous Studies and Sample Preparation

The SiC shell examined for this thesis came from a previous study of diffusion through SiC shells [4]. In the previous study, a total of 19 TRISO particles were exposed to varying fluences (Table 1.1). The C buffer layers and nuclear kernels of the TRISO particles were removed by laser drilling through the SiC shell and then leaching the particle in acid. The shells were repeatedly leached until a constant activity in the fission products of the SiC shell was measured [4]. At this point it was assumed that any remaining activity was due to daughter products which had migrated into the SiC shell and which would not be removed by leaching. The shells were then analyzed to determine the total number of the various daughter products in each shell (see Table 1.1). This method provides an accurate absolute measurement of the total loading of radioactive elements but gives no information about the elemental distribution in the shell.

1.5 Significance of the Research

The ultimate goal of this research is to characterize the trace-element distribution in TRISO SiC shells. The measured elemental distribution of fission products and/or trace elements in a nuclear fuel shell can then be correlated to observed defects and flaws in the shell, which can aid in understanding how to improve the performance of the SiC barrier layer. This information can be used to improve the design and performance of

Table 1.1: Selected isotopes and irradiation conditions for irradiated TRISO particles [4].

Ball ID	**Kernel Type**	**Fluence (10^{25} n/m^2)**	**Atoms in particles**		
			Cs-137	**Ce-144**	**Eu-154**
6151-23-020-C	UC_2	6.4	9.91(15)	4.95(15)	1.04(14)
6151-23-020-D	UC_2	6.4	1.01 (16)	5.58 (15)	1.14 (14)
6151-23-020-E	UC_2	3.5	7.69 (15)	4.37 (15)	1.02 (14)
6151-23-020-F	UC_2	3.5	7.82 (15)	4.39 (15)	9.11 (13)
6157-08-020-A	UCO	5.8	9.05 (15)	4.36 (15)	1.19 (14)
6157-08-020-B	UCO	5.8	9.14 (15)	4.38 (15)	1.05 (14)
6157-11-020-A	UCO	6.1	9.52 (15)	4.60 (15)	1.10 (14)
6157-11-020-B	UCO	6.1	9.55 (15)	4.89 (15)	1.20 (14)
6252-12-COMP-A[1]	ThO_2	1.9	6.81 (14)	1.37 (14)	2.96 (12)
6252-12-COMP-B	ThO_2	1.9	6.56 (14)	1.36 (14)	3.56 (12)
7544-1-COMP-A	UC_2	1.9	2.79 (15)	5.71 (14)	2.20 (13)
7544-1-COMP-B	UC_2	1.9	3.22 (15)	6.30 (14)	2.16 (13)

[1] Used in this experiments of this thesis.

future nuclear fuels of power reactors and to better quantify the risks and performance expected with TRISO based fuels.

In the past, mainly destructive methods were used to obtain information at certain cross sectional locations of the fuel. With current strict environmental regulations and codes, performing destructive tests on radioactive materials is becoming extremely difficult, laborious and expensive. Moreover, the destructive tests as mentioned previously can smear elemental distributions and can distort or introduce damage and flaws in the sample. Fluorescence microtomography, on the other hand, offers a new nondestructive method to obtain the aforementioned information in 3-D.

This research also can be used to improve and enhance the measurement technique of fluorescence microtomography which is an emerging tool with potential and capabilities which are not yet fully explored. It should be noted that only a handful of publications are available in the area of fluorescence microtomography as applied to materials science.

1.6 Organization of the Thesis

After this introductory chapter, Chapter 2 describes the method of computed tomography with a particular emphasis placed on the fluorescence tomography technique. Also presented in this chapter are back- projection of filtered projection algorithm, factors affecting image qualities, and a qualitative comparison between sensitivity in transmission and fluorescence microtomography methods. Chapter 3 describes the experimental setup, instrumentation, fluorescence microtomography experiments, and

typical measured data. Tomographic data and image reconstruction results of the elemental distribution in the SiC shell are discussed in Chapter 4. Concluding remarks and future work are discussed in Chapter 5. Brief descriptions of synchrotron radiation sources and beamline 2-ID of the APS are given in Appendix A. Appendix B briefly describes the numerical and computer implementation of backprojection of filtered projection algorithm used in this research. Listing of computer programs is presented in Appendix C.

CHAPTER 2

X-RAY MICROTOMOGRAPHY

2.1 Introduction

The theory and practice of x-ray microtomography are very similar to those of x-ray computerized tomography (CT) used in medical applications. The major differences are the spatial resolution (the sampling interval) and the x-ray source. In microtomography, the resolution is on the order of micron and the x-ray source is a high brilliance synchrotron source, whereas in medical tomography the resolution is at most hundreds of microns and the x-ray source is a conventional x-ray tube. This chapter provides a brief description of x-ray computerized tomography, typical instrumentation for fluorescence microtomography, mathematical representation of computed tomography, and image reconstruction algorithms. In particular, it describes the backprojection of filtered projection scheme used in this research work. A review of factors influencing the image reconstruction quality is also provided.

2.2 X-ray Computerized Tomography

X-ray computerized tomography (CT) is a nondestructive and non-invasive method for internal imaging of an object's structure. In this method, a 2-D internal image is reconstructed from a finite number of 1-D projection images. A 3-D image can then be

reconstructed by simply stacking up the 2-D images obtained at pre-specified intervals in a direction perpendicular to the planes of 2-D images. The fact that computerized tomography works at all is one of the great triumphs of modern science; Radon transforms prove that in general an infinite set of (n-1)-D projection images are needed to reconstruct an n-D image in CT methods [11]. Yet in practice, detailed images can be reconstructed and the theory of tomography reconstruction led to the Nobel prize in 1979.

Computerized tomography is divided into two general categories: (1) transmission tomography and (2) fluorescence (emission) tomography. In transmission tomography, the x-ray beam is attenuated as it passes through the object's medium and reaches the detector located downstream of the sample (Fig. 2.1). The projection data obtained in this method represent the object's absorption density along the beam path. By rotating and translating the object or the beam at pre-specified projection angles, a set of projection data are obtained that can be used to reconstruct an image of the density and/or attenuation coefficient distribution of the object. In transmission tomography, usually, an area detector such as charged coupled detector (CCD) or a linear detector such as a PIN diode array with a spatial resolution less than or equal to the sampling interval are utilized for data collection.

In fluorescence or emission tomography, a detector located at ~90° to the x-ray beam measures the emitted photons from the internal sources (e.g.; trace elements) in the object (Fig. 2.1). The positioning of the detector in this way improves the measurement

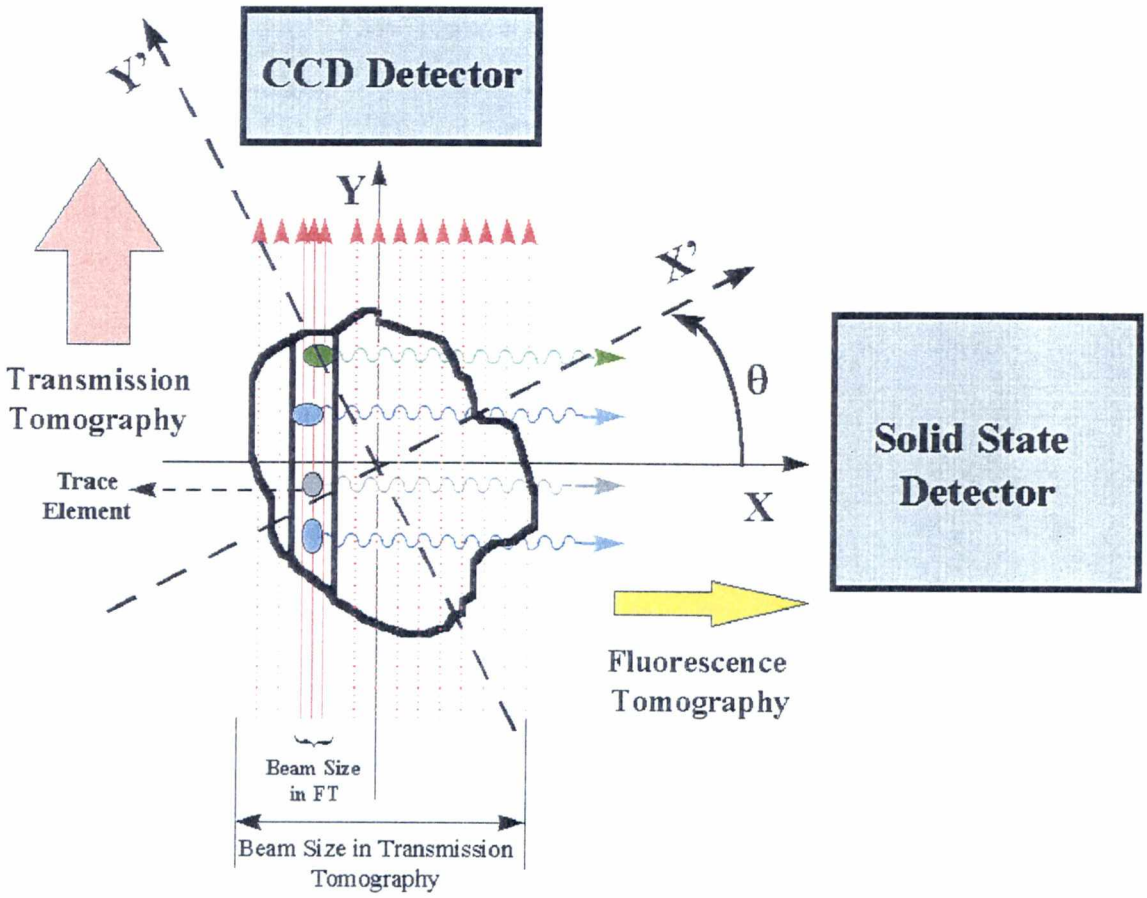

Figure 2.1: Schematic diagram of data collection in transmission tomography and fluorescence tomography.

efficiency and minimizes x-ray elastic and Compton scattering background with plane polarized radiation The type of detector is usually a point detector that measures only a single photon at a time for a given energy. As a result, the data collection rate is much slower than with transmission tomography. The projection data in fluorescence tomography corresponds to the concentration of emitting sources along the path of the incident x-ray beam. The projection data sets obtained at various projection angles are used to reconstruct the intensity or concentration images of the emitting sources (e.g.; trace elements) in the sample under study.

2.3 Basic Instrumentation of X-ray Fluorescence Microtomography

The major instruments used in a typical fluorescence microtomography experiment include the necessary tools to focus the x-ray beam, to hold and move the sample, to acquire the fluorescence projection data, and to measure the incident x-ray beam. Figure 2.2 shows a schematic diagram of a typical experimental setup used in fluorescence microtomography measurements. The setup includes an x-ray beam from a synchrotron source, a precision translation and rotational stage, focusing optics, a solid state detector, and an ion chamber.

The synchrotron source provides a very intense linearly polarized and highly collimated x-ray beam that can be focused to micron or submicron sizes as it passes through the focusing optics and reaches the sample. There are many emerging microbeam focusing systems capable of achieving submicron x-ray beams [3,12]. The most advanced methods of focusing optics for x-ray micro beams are:

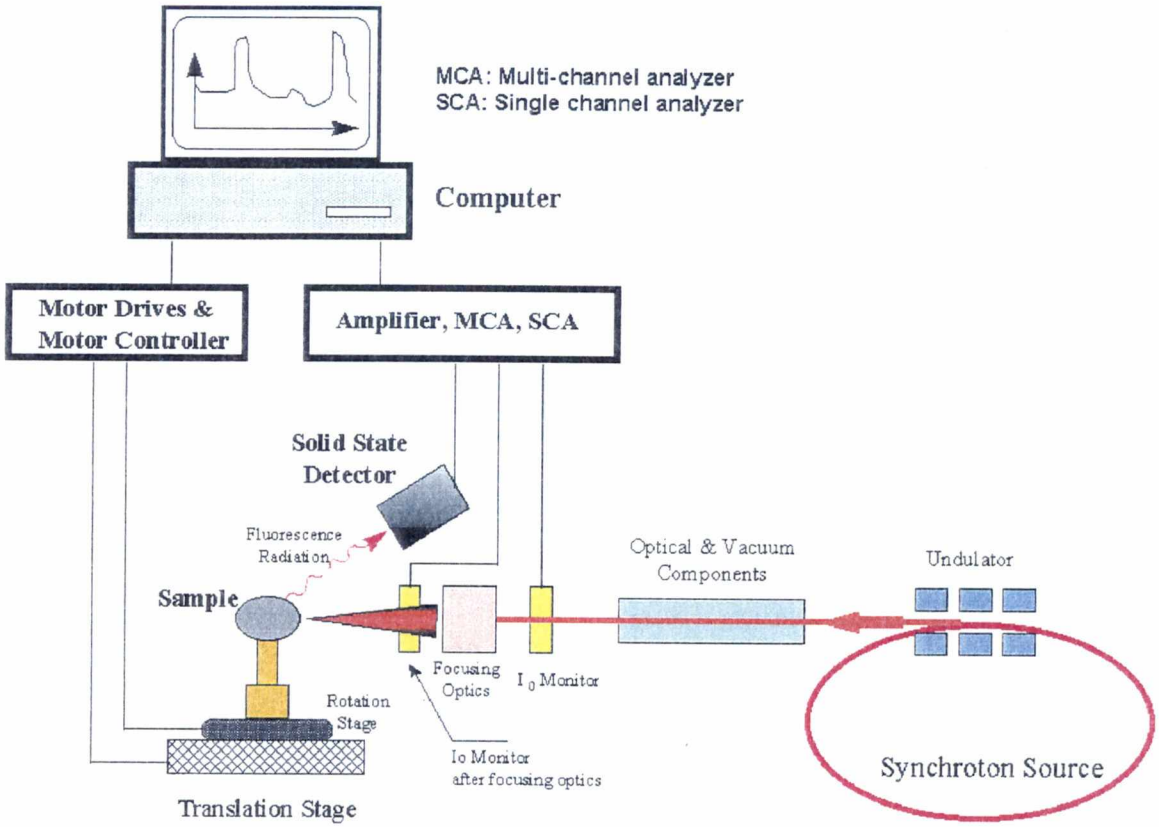

Figure 2.2: Schematic diagram of a typical experimental setup for fluorescence microtomography measurements.

1. Kirkpatrick Baez (KB) mirrors
2. Fresnel Optics
3. Capillary Optics

Other choices include multi element refractive lens, Bragg crystals and Bragg-Fresnel optics. References [3,12] provide a detailed description with advantages and disadvantages of each group as used in x-ray synchrotron applications. For these focusing optics, investigators have reported micron and submicron resolution in an energy range of 6-30 keV. For example, KB mirrors, Fresnel optics, and capillary optics have the achieved resolution of 0.7 μm, 0.07 μm, and 0.05 μm [3,12], respectively. It should be pointed out that currently, there is an ongoing revolution in x-ray optics and as a result, x-ray beam area is decreasing by a factor of 4 every 3-5 years. Figure 2.3 shows the steadily decreasing trends in x-ray beam area over the last decade. In this experiment a high-performance Fresnel zone plate was used to focus the x-ray beam.

The translation and rotation stage holds the sample and provides micron and submicron step size movements. A typical stage utilizes precision stepping motors under computer control to rotate and translate the sample with very precise (~0.1 μm) step sizes. Even more advanced stages utilize optical encoder technology to achieve ~25 nm bi-directional movements over centimeters of travel.

The detector is normally a high energy-resolution solid-state detector with a good counting efficiency. The detector's electronics should provide a high signal-to-noise

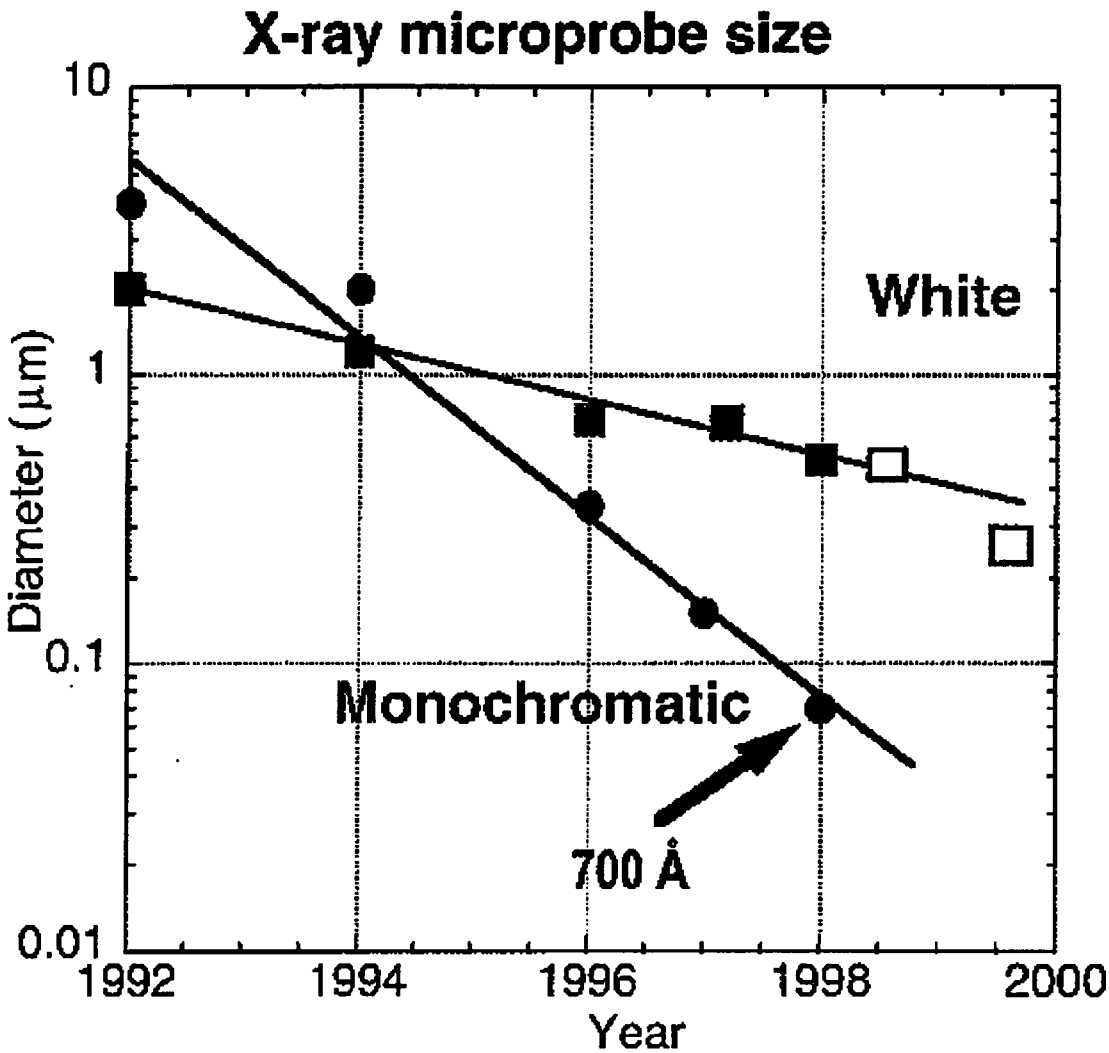

Figure 2.3: Changes in x-ray beam size over the last decade [15].

ratio, good dynamic range, a wide range of linearity, and a small dead time. These characteristics are important both for the fluorescence measurements of elements with a close energy spacing and for avoiding problems such as detector saturation and pileup effects. A typical solid state detector with a Germanium or Silicon crystal has an energy resolution of ~120 eV, a counting rate of ~10,000 pulses/sec, and a detector efficiency of ~85%.

The Ion chamber is used to monitor the x-ray beam intensity during the experiment. Relative beam intensity is required to normalize the projection data before they can be used in the image reconstruction algorithms. It should be noted that the synchrotron x-ray beam has a complicated time dependence dominated by an exponential decay of intensity (see Fig. 2.4) which makes the incident beam monitor essential [13,16].

2.4 Mathematical Representation of Computed Tomography

Figure 2.5 schematically illustrates the general concept of computerized tomography. As shown, in transmission tomography, the penetrating x-ray is attenuated point-by-point as it passes through the object and reaches the detector. The detector measures the transmitted x-ray intensity, I_μ, which is estimated as follows:

$$I_\mu(t,\theta) = \int S(E) e^{-\int \mu(x,y,E)ds} dE \qquad (2.1)$$

Here, S(E), is the energy spectrum of the incident x-ray beam and $\mu(x,y,E)$ is the attenuation coefficient along the y direction. For a monochromatic x-ray beam with energy E_0, the energy spectrum can be written as a delta function which simplifies

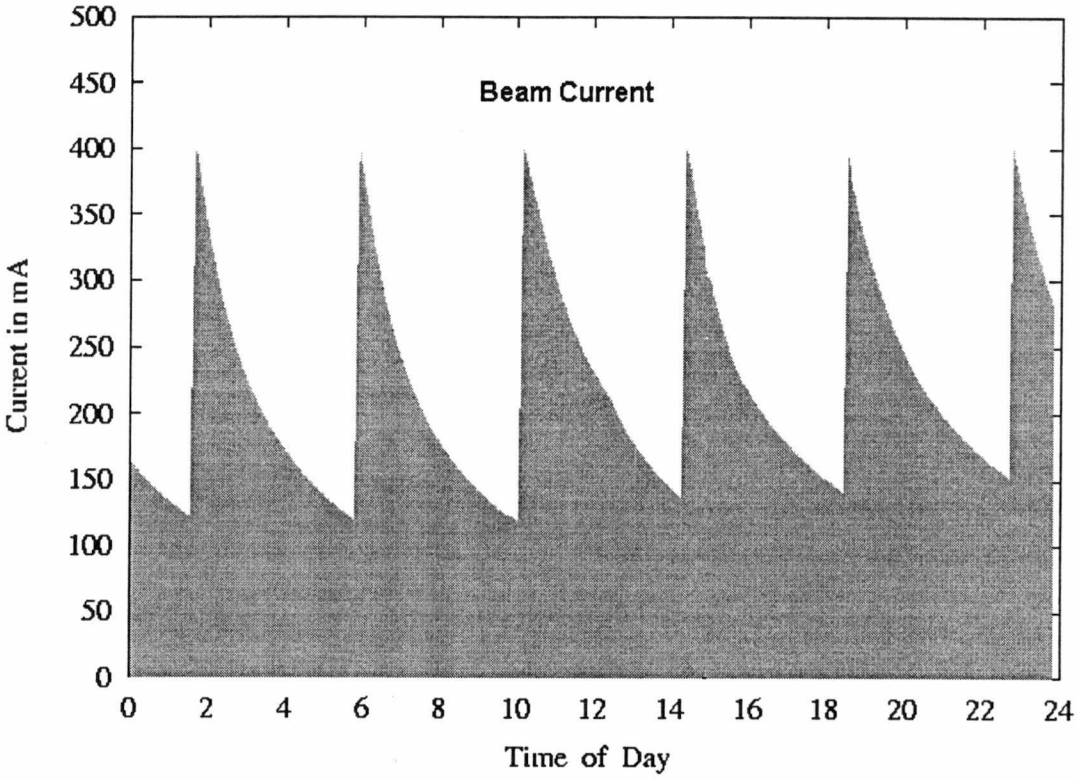

Figure 2.4: Decay of beam current (intensity) with time[2].

[2] Taken from the Advanced Light Source (ALS) Web site (www.als.lbl.gov)

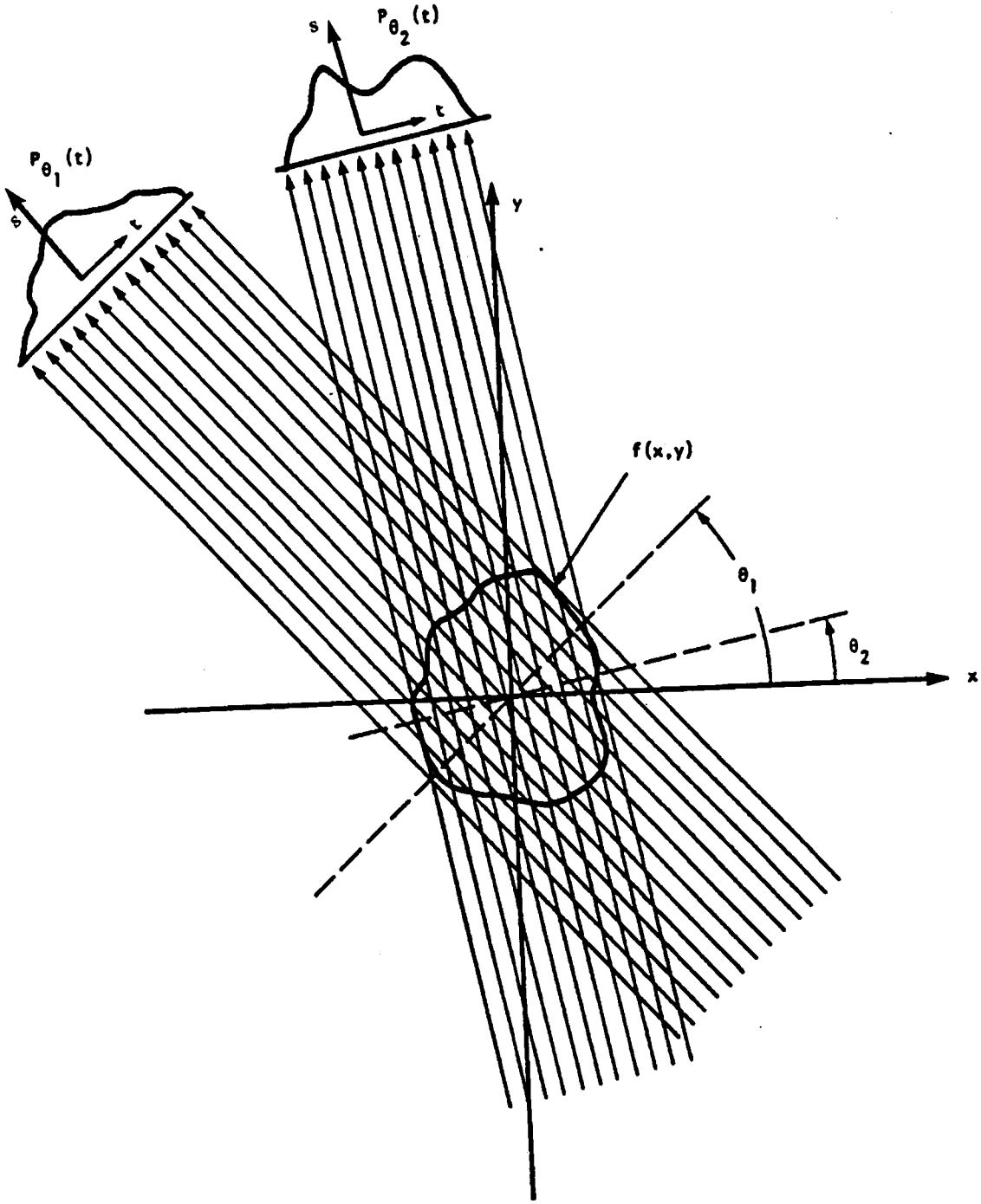

Figure 2.5: Data collection in transmission tomography [21].

Equation (2.1) to the following form.

$$S(E) = I_0(E_0)\delta(E - E_0)$$
$$I_\mu(t,\theta) = I_0 e^{-\int \mu(x,y,E_0)ds} \tag{2.2}$$

Here, I_0 is the incident x-ray intensity. The projection data, P, at the projection angle θ is then defined as:

$$P(t,\theta) = \ln(\frac{I_0}{I_\mu}) = \int \mu(x,y,E_0)\ ds \tag{2.3}$$

In fluorescence tomography, the projection data is derived in a somewhat different manner (see Fig. 2.6). We consider two limits in deriving the projection data. In the first case, it is assumed that the attenuation of fluorescence photons from the fluorescence sources in the object to the detector is negligible. This means that the object's attenuation coefficient, $\mu(x,y)$, is very small in the fluorescence energy range of interest. In the second case, the effects of object's medium on the attenuation of photons are taken into account, but the sample is assumed to have the same absorption for each volume element.

Case 1: $\mu(x,y) \cong 0$

$$I_F(y',\theta) = \int\int S(E,x',y')dEdx' \tag{2.4}$$

Here, $I_F(y',\theta)$ is the fluorescence intensity measured by the detector and $S(E,x,y)$ is the fluorescence source within the object. Since the incident beam operates at a monochromatic energy, the fluorescence source, $S(E,x',y')$, can be written as:

$$S(E',x',y') \approx I_0(E_0)\Omega\sigma(E_0)C(x',y') \tag{2.5}$$

Here $C(x',y')$ is the elemental concentration of the fluorescence source, $\sigma(E_0)$ is the fluorescence cross section at the incident beam energy, and Ω is the detector solid angle.

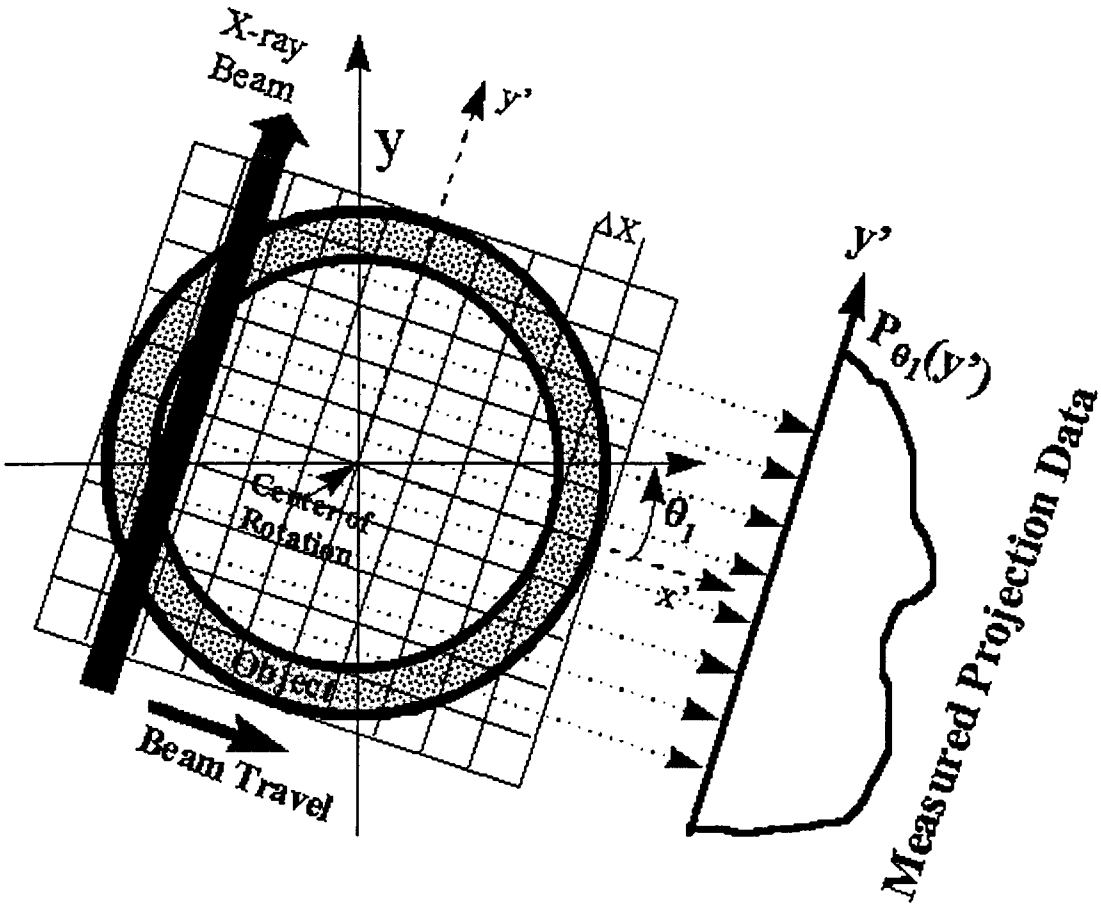

Figure 2.6: Data collection in fluorescence microtomography.

Thus, Eq.(2.5) can be simplified as follows.

$$I_F(y',\theta) = I_0 \int \rho(x',y')dx' \qquad (2.6)$$

where, $\rho(x',y') = \Omega\,\sigma\,C(x',y')$ corresponds to the 2-D concentration distribution of the fluorescence source within the object, and $P(y',\theta) = I_F(y',\theta)/I_0$ is the projection data at angle θ.

Case 2: $\mu(x,y) \neq 0$

In many cases however, attenuation by the sample is not negligible. The introduction of the attenuation coefficients into the Equation (2.6) makes the treatment of the integral more difficult since the coefficients in general can change with both x and y positions. Nevertheless, for many applications such as measurement of trace elements in an otherwise uniform matrix, the assumption of a constant attenuation coefficient provides reliable results. The following equations show how to incorporate the effects of attenuation coefficients into the fluorescence projection data.

$$P(y',\theta) = \frac{I_F(y',\theta)}{I_0} = \int \rho(x',y')l(x',y')dx' \qquad (2.7)$$

where $l(x',y') = e^{-\int_x\int_y \mu(x',y')dx'}$ compensates for the photon attenuation from the fluorescence source to the detector. For a constant attenuation coefficient, Equation (2.7) can be written as:

$$P(y',\theta) = \frac{I_F(y',\theta)}{I_0}\exp^{\mu l'} = \int \rho(x',y')dx' \qquad (2.8)$$

If the attenuation coefficients cannot be assumed constant, transmission tomography is needed to determine the values of the coefficients at each (x,y) position [17]. References

[17-19] elaborate in more details the effects of attenuation coefficients on the image reconstruction of emission tomography problems particularly for medical applications.

2.5 Image Reconstruction Algorithms

The problem of image reconstruction in computed tomography involves the calculation of spatial distributions $\mu(x,y)$ or $\rho(x,y)$ from the measured projection data sets, $p(t,\theta)$ or $p(y',\theta)$ as shown in Equations (2.3), (2.6), or (2.8). Radon inverse transform can treat this inverse problem with the following equation [17].

$$\mu(x,y) = -\frac{1}{2\pi^2}\lim_{\varepsilon\to 0}\int_{\varepsilon}^{\infty}\frac{1}{t}\int_{0}^{2\pi} p_1(x\cos\theta + y\sin\theta + t,\theta)\,d\theta dt \tag{2.9}$$

where $p_1((x\cos\theta + y\sin\theta + t) = l,\ \theta)$ is the partial derivative of $p(l,\theta)$ with respect to l (see Fig. 2.7). Note that the projection data $p(t,\theta)$ is expressed in the polar system which is needed to solve the reconstruction problem. The above equation uniquely determines the distribution map of attenuation coefficients from the set of all its line integrals. Figure 2.7 shows the polar coordinate system for the image reconstruction in computed tomography applications.

However, the Radon transform shown in the above form cannot be used directly in CT applications since it requires an infinite set of projection data. In CT methods, the data set is finite and includes inaccuracies due to noise and measurement errors to which the

transform is sensitive. Therefore, best approximation solutions similar to the least squared method are needed to perform the image reconstruction.

There are two general classes of reconstruction algorithms for both transmission and fluorescence computed tomography: (1) analytical methods and (2) iterative methods. With analytical methods, the model equation (e.g.; Eqs. (2.3), (2.6), or (2.8)), which is used for the estimation of projection data, is inverted to obtain the distribution of attenuation coefficients or elemental concentration. The prime examples of such methods are backprojection of filtered projection algorithm and 2-D Fourier slice technique.

With the iterative methods, first the distribution map of the attenuation coefficients or elemental concentration is predicted and then a model equation such as Eqs. (2.3), (2.6), or (2.8) is employed to estimate the projection data. The difference between the estimated and measured projection data is used to iteratively refine the distribution map. A notable example of iterative methods is the Maximum Entropy Algorithm (see references [17,19]).

Analytical methods are computationally much more efficient and conceptually easier to understand than the iterative methods. However, the iterative methods can treat physical problems such as measurement noise, object motion, and beam hardening effects much better than analytical methods. References [17-19] should be consulted for detailed information about the theory and application of analytical and iterative methods.

2.5.1 Backprojection of Filtered Projection Algorithm

Back-projection of filtered projection algorithm is basically a formalism for deducing the density of an object from projection data using Fourier transforms. It is currently the most widely used algorithm for x-ray tomography applications. The algorithm is accurate, robust, and easy to understand and implement.. The sequence of steps to implement the back-projection of filtered projection algorithm includes: (1) the Fourier transform of the projection data in polar coordinates, (2) the coordinate transform from polar to rectangular, (3) frequency filter multiplication, (4) inverse Fourier transform, and (5) back-projection of the modified projection data. The above sequence can be symbolically summarized as follows [19].

$$X = back - project\{F_1^{-1}[\tilde{c}\,F_1(p)]\} \tag{2.10}$$

Here X is the distribution map, p are the projection data, c is the filter function, and F_1 is the 1-D Fourier transform. The rationale for using a filter function is to reduce the high frequency noise components in the reconstructed image, to improve signal-to-noise ratio, and to some degree compensate for a finite number of projection data set and deficiencies in sampling at high frequencies. Figure 2.8 illustrates image reconstruction of a central point object using back-projection of filtered projection. As can be seen in the figure, the projection data are convoluted with a filter function and then back-projected to reconstruct the image by summing contributions from all projection data obtained at various projection angles. The reconstructed image includes ray type artifacts which is due to a very small number of projections. Thus, filtering of the projections cannot fully compensate for artifacts when the number of projections is too small.

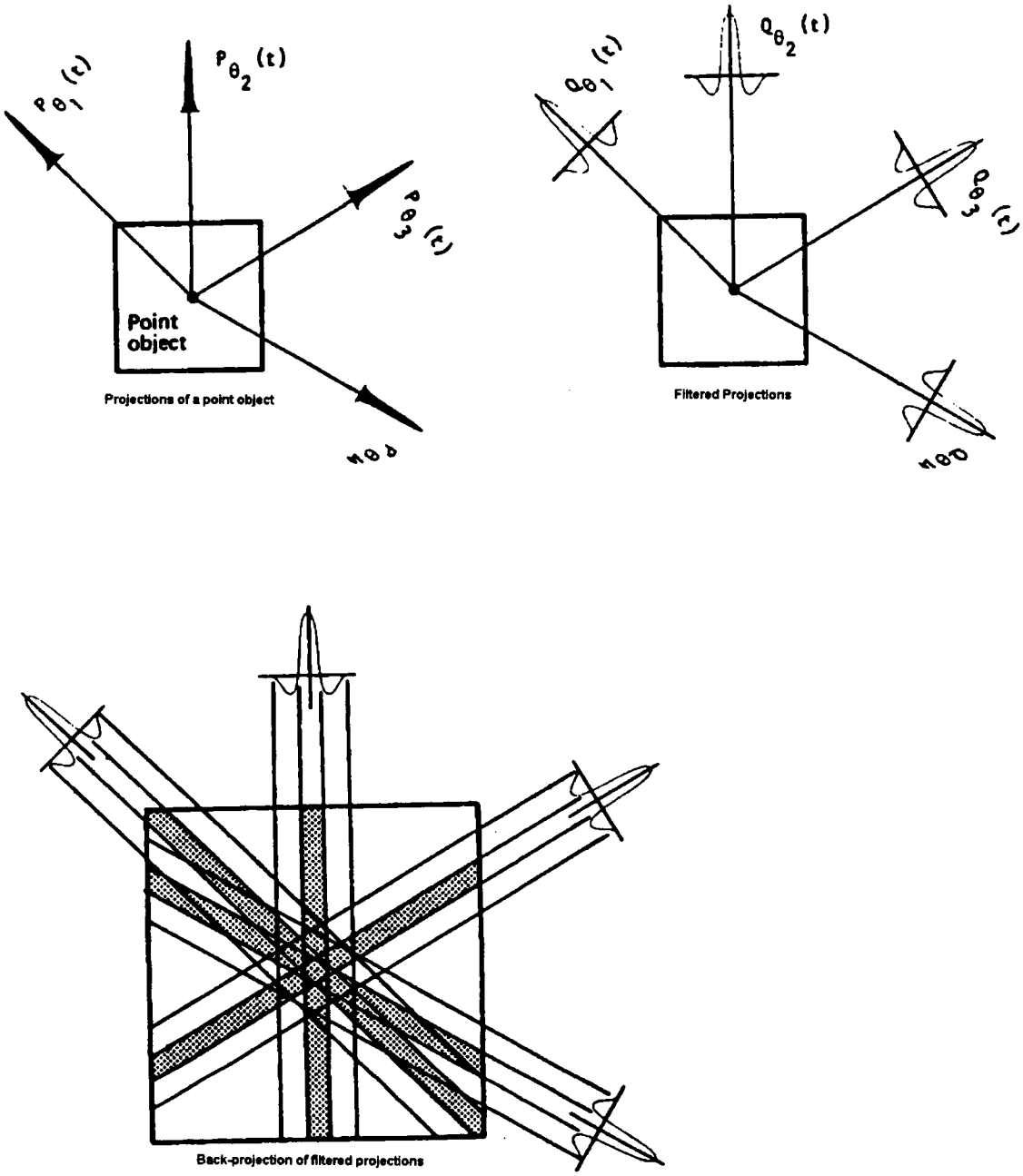

Figure 2.8: Artifacts produced in image reconstruction of a central point using back-projection of filtered projection algorithm [21].

The mathematical representation of back-projection of the filtered projection is as follows. First, the Fourier transform of the projection data is taken. The (measured) projection data in the polar (or rotated) coordinates (see Fig. 2.9) is defined as;

$$P(t,\theta) = \int_{-\infty}^{+\infty} \mu(t,s)ds \tag{2.11a}$$

The Fourier transform of the above equation is:

$$P_F(\theta,\omega) = \int_{-\infty}^{+\infty} P(t,\theta)e^{-i\omega t}dt = \int_{-\infty}^{+\infty}\int_{-\infty}^{+\infty} \mu(t,s)e^{-i\omega t}dsdt \tag{2.11b}$$

where P_F denotes the Fourier transform of the projection data in the rotated coordinates and ω is the spatial frequency. The polar coordinates (t, s) are related to the rectangular coordinates (x, y) by

$$\begin{pmatrix} t \\ s \end{pmatrix} = \begin{pmatrix} \cos\theta & \sin\theta \\ -\sin\theta & \cos\theta \end{pmatrix}\begin{pmatrix} x \\ y \end{pmatrix} = \begin{pmatrix} x\cos\theta + y\sin\theta \\ -x\sin\theta + y\cos\theta \end{pmatrix} \tag{2.12}$$

Then, Equation (2.11b) is transformed to (x, y) coordinates using Equation (2.12).

$$P_F(\theta,\omega) = \int_{-\infty}^{+\infty}\int_{-\infty}^{+\infty} \mu(x,y)e^{-i\omega(x\cos\theta + y\sin\theta)}dxdy \tag{2.13}$$

Next, the integrand of the above equation is multiplied by the filter function, $|\omega|g(\omega)$, and then the inverse Fourier transform of the resulting equation is taken to determine the density map[3], $\mu(x,y)$.

$$\mu(x,y) = \int_{0}^{\pi}\int_{-\infty}^{+\infty} P_F(\omega,\theta)e^{i\omega(x\cos\theta + y\sin\theta)} \mid \omega \mid g(\omega)d\theta d\omega \tag{2.14}$$

The filter function, $|\omega|g(\omega)$, is mathematically defined as a product of a ramp function $|\omega|$

[3] See reference [20,23] for details of the derivation.

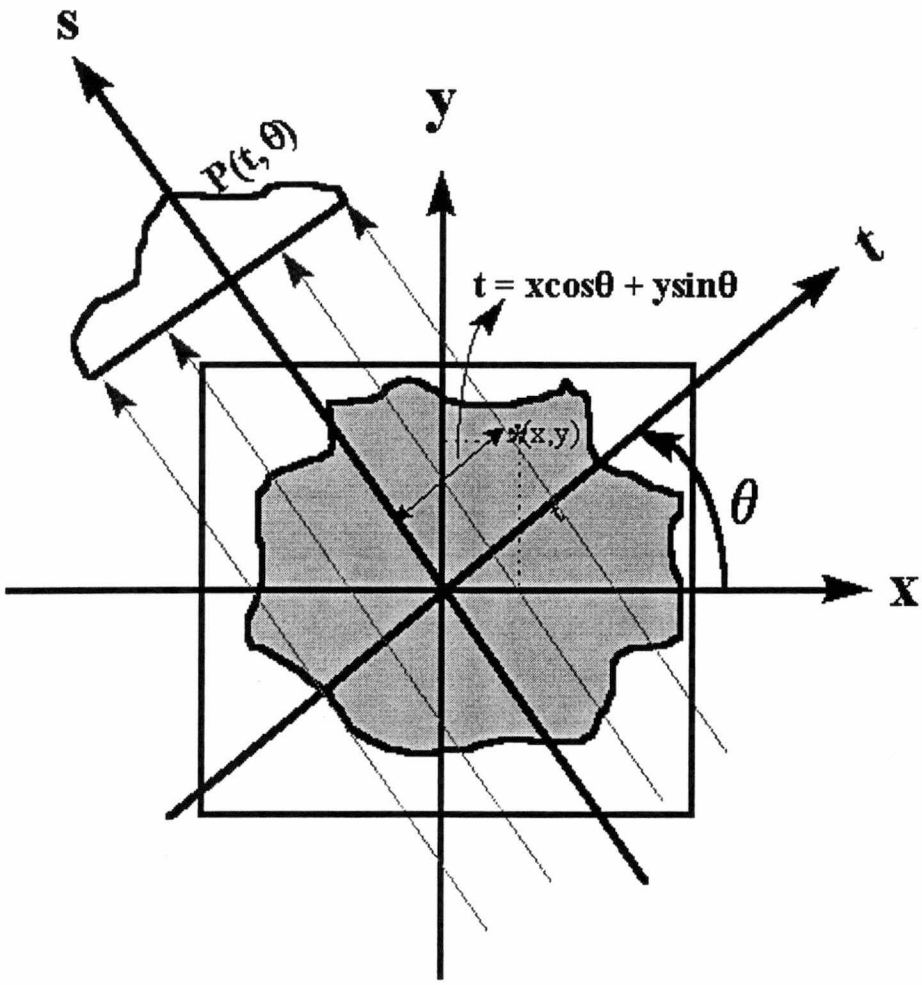

Figure 2.9: The coordinate system used for the back-projection of filtered projection [21].

by a window function g(ω) in frequency space. Typical filter functions used in the algorithm are Han, Ham, Parzn, and Butterworth. A brief description of each filter with mathematical representation is given here. References [17-19] should be consulted for more details.

Ham Filter

Ham filter is a low-pass frequency filter, and it is defined as the product of the Hamming window, g(ω), by the ramp function, |ω|.

$$g(\omega) = \begin{cases} 0.54 + 0.46\cos \pi\omega / \omega_m, & \text{if } |\omega| \le \omega_{\mathrm{m}} \\ 0 & \text{if } |\omega| > \omega_{\mathrm{m}} \end{cases} \tag{2.15}$$

Here ω_m is the cutoff frequency which is an input parameter with a typical value of 0.5. The mathematical representation of the Ham filter is as follows.

$$c(\omega) = \begin{cases} 0.54|\omega| + 0.46|\omega|\cos \pi\omega / \omega_m, & \text{if } |\omega| \le \omega_{\mathrm{m}} \\ 0 & \text{if } |\omega| > \omega_{\mathrm{m}} \end{cases} \tag{2.16}$$

Han Filter

Han filter is almost identical to the Ham filter but the filter parameters are slightly different. It is defined as

$$c(\omega) = \begin{cases} 0.5|\omega| + 0.5|\omega|\cos \pi\omega / \omega_m, & \text{if } |\omega| \le \omega_{\mathrm{m}} \\ 0 & \text{if } |\omega| > \omega_{\mathrm{m}} \end{cases}. \tag{2.17}$$

Parzn Filter

Parzn filter is mathematically defined as

$$c(\omega) = \begin{cases} |\omega| - 6|\omega|\left(\frac{|\omega|}{\omega_m}\right)^2\left(1-\frac{|\omega|}{\omega_m}\right) & \text{if } |\omega| \le \omega_m / 2 \\ 2|\omega|\left(1-\frac{|\omega|}{\omega_m}\right)^3 & \text{if } \omega_m < |\omega| \le \omega_m \\ 0 & \text{if } |\omega| > \omega_m . \end{cases} \tag{2.18}$$

Butterworth Filter

Butterworth filter includes an additional parameter which defines the order of the filter. This parameter can be used as an input variable to control the shape of the filter. The Butterworth filter is mathematically defined as

$$C(\omega) = \frac{|\omega|}{\sqrt{1+(|\omega|/\omega_m)^{2n}}} \tag{2.19}$$

Here, n is the order of the filter. The typical range of n used in reconstruction algorithms is from 2.5 to 175 and the frequency parameter, ω_m, is from 0.25 to 1. Butterworth filter has the maximum flatness around zero frequency as compared to other filters.

The shapes of window functions and their corresponding filter functions are shown in Fig. 2.10. Since there is always a trade off between a good image resolution and a reduction in the reconstructed noise level, the choice of the filter becomes application dependent. For example, Parzn filter suppresses the noise level more than both Ham and Han filters but in the expense of image resolution. Butterworth filter may optimally reduce the noise level without sacrificing the image resolution. However, it requires an

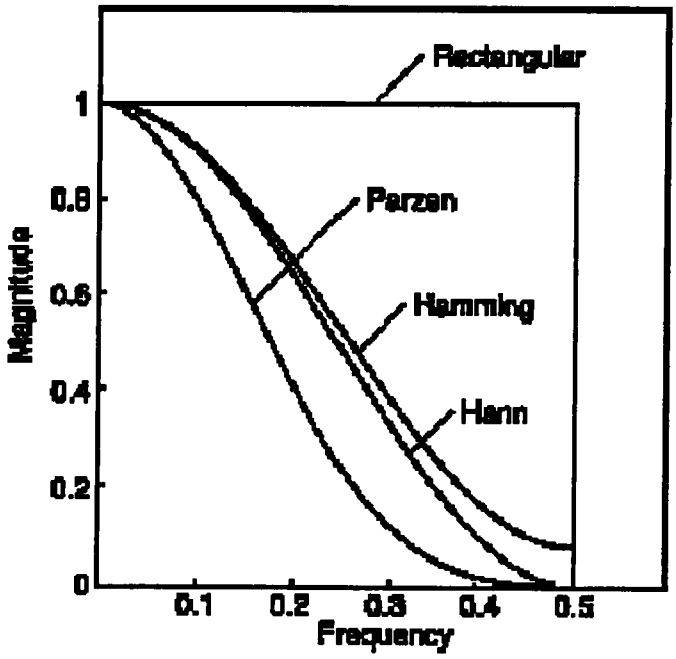

Window Functions

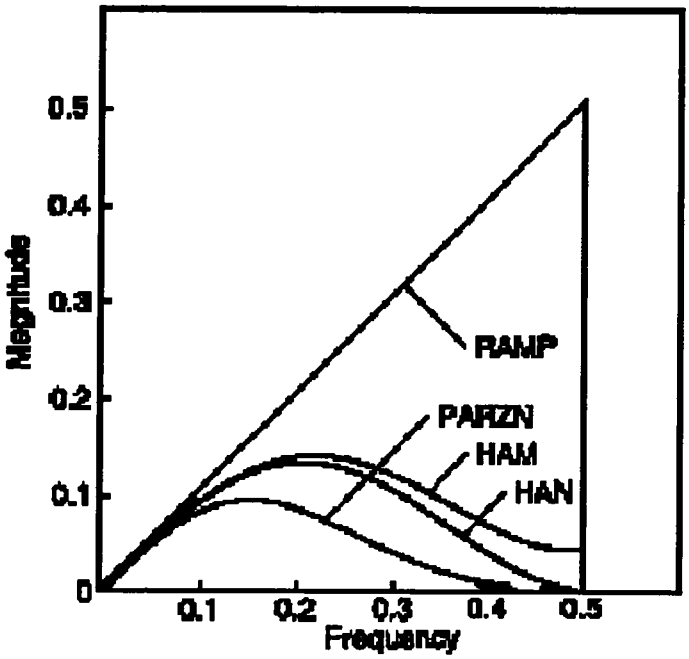

Filter Functions

Figure 2.10: Frequency characteristics of window functions and filter functions [19].

elaborate trial and error procedure to obtain optimal values for the filter parameters namely, the filter order and the cutoff frequency.

The digital implementation of the back-projection of the filtered projection algorithm is shown in the Appendix B and extensively described in references [17-19]. The computer implementation of the algorithm in Matlab software is also shown in the Appendix B.

2.6 Factors Influencing the Image Reconstruction Quality

Spatial resolution and sensitivity are the two main factors that evaluate the quality of a reconstructed image in CT methods [11]. This is especially true when fluorescence microtomography is used for imaging of elemental distribution of micron- size particles (trace elements) in an object. The spatial resolution, δx, in fluorescence tomography is the step size corresponding to the bigger of x-ray probe size or the object's sampling interval or mesh size[4]. The sensitivity, dC/C, measures how well the reconstructed image can show small changes in the elemental concentration of the object. Factors such as signal-to-noise ratio, reconstruction algorithm, measurement noise, and beam hardening effects can greatly influence the quality of a reconstructed image in terms of both spatial resolution and sensitivity. One way to minimize the influence of such factors, is to use a large set of projection data. This requires additional measurement time which may be difficult to obtain due to the demand for limited synchrotron beamtime. In addition, a long experiment has additional risk because of possible downtimes in synchrotron facilities. Thus, the number of projection data must be optimized to obtain

the desired image quality within a reasonable experiment time. Reference [11] presents an optimal relationship between the sampling points M (grid size) and the projection number, N;

$$N \approx \frac{\pi}{2} M \,. \tag{2.20}$$

The grid size, M, is equal to 2R/Δx where R is the maximum length of the sample from the center of rotation and Δx is the sampling interval (mesh size). If a value of N satisfies the above relationship, then the image quality improves. Otherwise, the image quality could be degraded because of noise, artifacts, or a small set of projection data. The complete derivation of Eq.(2.20) is shown in reference [11].

Other methods of improving image quality include preprocessing of the projection data to remove possible artifacts, repeat of the experiment to achieve a better photon counting statistics, and the application of proper frequency filters in the reconstruction algorithms to reduce the high frequency noise components of the reconstructed image with a minimum degradation of spatial resolution. The latter method is normally achieved through a trial and error procedure.

2.7 Qualitative Comparison between Elemental Sensitivity in Transmission Microtomography and Fluorescence Microtomography

As pointed out earlier, the main advantage of fluorescence microtomography method over transmission microtomography is that the sensitivity in the fluorescence method is much

---

[4] Usually, these two numbers are equal. Note that the maximum achievable resolution depends always on the x-ray probe size.

greater than that in the transmission method for elemental distribution of high Z trace elements in a low Z matrix. To clarify this advantage, a qualitative comparison is made between the elemental sensitivity of fluorescence and transmission tomography. For example, in transmission tomography, the most sensitive way to measure the elemental distributions is to compare the transmitted beam intensity between x-ray energies above and below the absorption edge of a trace element. Figure (2.11) illustrates a transmission tomography experiment in which the transmitted beam intensity is attenuated along the volume elements in the sample matrix and is detected with an area detector. The area detector is usually a CCD type with a typical resolution of 14-16 bits.

Table 2.1 shows that for the trace elements monitored in this research work the linear absorption coefficient increases by approximately a factor of 8 at the K absorption edge. Thus, for a small pixel with length ΔX (see Fig. 2.11) and trace-element concentration C_t, the transmitted beam intensity above the K absorption edge is attenuated by the amount of $f = e^{-7\mu_t \Delta X C_t}$ as compared to the transmission below the absorption edge. Here, μ_t is the trace-element linear absorption coefficient which is approximately estimated to be $2.310^{-3}Z^4$ (cm^{-1}) at x-ray energy below the absorption edge. The sensitivity of the measurement to the concentration of the trace element depends strongly on the resolution limit of the detector. The resolution limit for the transmitted beam in the most favorable case (but impractical) is when the CCD operates near the saturation limit. At the limit of detectability, the additional absorption is small and is at the limit of the resolution of the detector. This means that if the attenuation factor, f, is estimated as($e^{-\varepsilon} \sim 1-\varepsilon$), then the

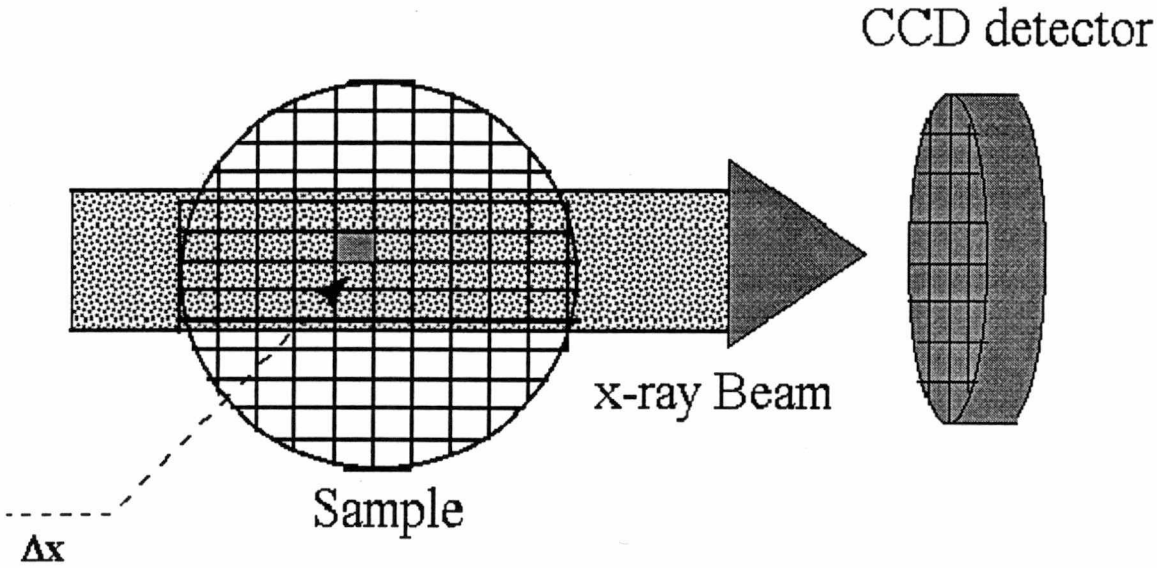

Figure 2.11: Attenuation of x-ray beam intensity in a transmission tomography.

Table 2.1: Linear absorption coefficients below and above the K absorption edge for the monitored trace elements in SiC shell of the TRISO fuel ball.

Element	**E_b (Energy below the K absorption edge (keV))**	**E_a (Energy above the K absorption edge (keV))**	**σ_b (Cross section at E_b (cm^2/g))**	**σ_a (Cross section at E_a(cm^2/g))**	**Ratio of σ_a/σ_b**
Ca	4.037	4.038	7.944×10^3	7.118×10^4	8.960
Cr	5.988	5.989	6.453×10^1	5.513×10^2	8.543
Fe	7.111	7.112	5.217×10^1	4.150×10^2	7.954
Ni	8.332	8.333	4.424×10^1	3.346×10^2	7.563
Cu	8.978	8.979	3.787×10^1	2.889×10^2	7.628
Zn	9.658	9.659	3.648×10^1	2.659×10^2	7.304
Ba	37.44	37.441	5.533	2.889×10^1	5.220
Cs	35.984	35.985	5.754	3.078×10^1	5.340

detector resolution should be approximately equal to ε to detect the trace-elements. Therefore,

$$7 \times 2.3 \times 10^{-3} Z^4 (cm^{-1}) \Delta X (cm^{-1}) C_t \sim 2^{-16}. \tag{2.21}$$

Simplifying the above equation and changing length units to microns gives the following relationship for trace element sensitivity in transmission tomography.

$$C_t \Delta X(\mu m) \sim \frac{9.5(\mu m)}{Z^4} \tag{2.22}$$

For example, with Z~26 and for feature size of ~1μm the estimated detectable limit cannot be less than 20 PPM.

For heavier elements such as fission products, it may not be possible to perform the experiment at K-edge energies because of limitations in the synchrotron x-ray beam energy. Performing the experiment at energies corresponding to the L edges could be difficult because the L lines can be masked by the fluorescence lines of lighter elements. In addition, the sensitivity degrades at the L edges since the cross section jump is approximately 2 times less than the cross section jump at the K edges.

In a real measurement the detectable limit must be much higher, since the CCD must operate away from the detector saturation limit to avoid non-linear performance and because of increased noise introduced in the reconstruction process.

By contrast, fluorescence tomography is much more sensitive to trace elements. The estimated minimum detectable limit (MDL) of a modern x-ray fluorescence microbeam is ~5-80 PPB/s/μm^2 for a uniform sample [10]. Since the MDL increases as the square-root

of the background, and decreases linearly with signal, the MDL of a small particle inside a larger sample will scale inversely with the ratio of particle size to sample size [10]. The estimated MDL for fluorescence x-ray microbeam is therefore ~500-8000 PPB/s/μm^2, or ~2 orders of magnitude better than for transmission microtomography. In actual tomographic reconstruction, the elemental sensitivity is degraded due to noise introduced by the reconstruction algorithm. Nevertheless, x-ray fluorescence tomography is at least 100-1000 times more sensitive to elemental distributions than transmission tomography.

CHAPTER 3

FLUORESCENCE MICROTOMOGRAPHY EXPERIMENT

3.1 Experimental Setup

The x-ray microtomography experiment was performed on beamline 2-ID of the Advanced Photon Source [25]. Beamline 2-ID uses a low bandpass x-ray mirror to define a beam axis and reduce the incident-beam thermal load. The mirror is followed by a novel Si 111 perfect crystal monochromator [25] and a hard x-ray zone plate. The x-ray energy was set at 10.5 keV. For this experiment a 40 cm focal length zone plate was used which produced a spot size of approximately 1x3 μm^2.

Figure 3.1 shows a schematic diagram of the experimental setup used to perform the fluorescence microtomography measurements. The setup is conceptually very simple, though, in practice great care is required to optimize the performance. The setup includes a hard x-ray zone plate, a sample holder, a rotation and translation stage, a solid state detector, a Pin Diode detector, and a computerized data acquisition system.

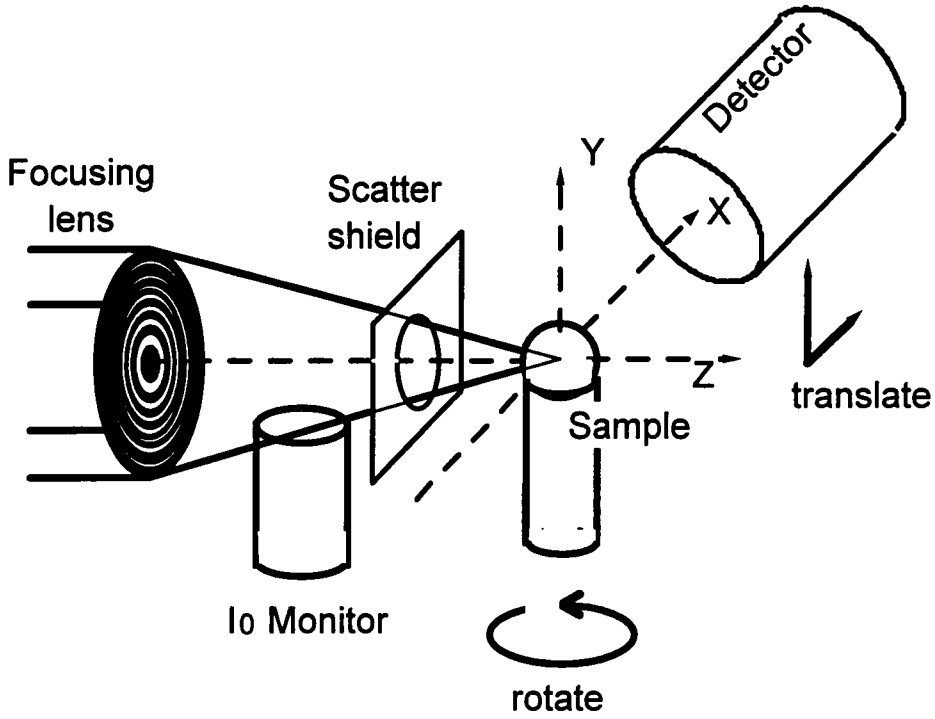

Figure 3.1: Schematic diagram of the experimental setup used to perform fluorescence microtomography experiments at beamline 2-ID of the APS.

The sample, TRISO fuel shell, was epoxied to a glass fiber and sandwiched between 2 mil kapton tape to simplify handling and to secure the sample. The fiber was mounted on a small goniometer head which allowed the fuel ball to be positioned at the center-of-rotation of the rotation stage. The ball was then centered on the x-ray beam so that the translation range of the measurement passed completely through the center of the ball.

An EG & G Si solid state detector with 200 eV energy resolution, an effective area of 110 mm^2, and a counting rate of 10,000 pulses/sec was placed at 90° to the incident beam. The distance between the detector and the sample was set to be approximately 3 centimeter. This detector geometry allows efficient measurement of the characteristic fluorescence from the trace elements while minimizing the x-ray elastic and Compton scattering.

Because a tomographic reconstruction requires consistent measurement conditions, an accurate measurement of the incident beam intensity was needed. However, at the time of experiment, the beamline was not equipped with any measuring device of the incident beam after the zone plate. A small AMPTEC model XR-100T PIN Diode detector with 250 eV energy resolution [22] was therefore inserted along the optical train as a beam monitor. The detector was placed at ~90° 2θ to the beam but out of the plane of the x-ray ring (to optimize scattering efficiency). Scatter from the air between the sample and the zone plate was monitored. This crude incident beam monitor worked well after a backscatter shield was installed between the sample and the air volume viewed by the detector (see fig. 3.1). In a previous fluorescence tomography attempt with the same

sample, the measurements were rendered useless for reconstruction by large and unmonitored variations in the incident beam intensity. Figure 3.2 shows the variations in the incident beam intensity during the fluorescence microtomography experiment. As shown in Fig. 3.2 the observed variations are large and must be included in the data analysis to obtain a reliable reconstruction.

3.2 X-ray Fluorescence Microtomography Experiment

The x-ray fluorescence measurements on the fuel shell were conducted in three phases. In the first phase, the unfocused beam was centered on the fuel ball shell to determine the detectable trace elements. As shown in Fig. 3.3, the incident 10.5 keV beam excited fluorescence spectrum from ~3-10.5 keV. With the aid of a characteristic emission table, the trace elements in the shell were identified and then marked on the figure. In the spectrum, the elastic and Compton scattering peak was observed at 10.5 keV which corresponded to the incident beam energy. Using the obtained spectrum, regions-of-interests (ROIs) were set around the dominant fluorescence lines. Because of limitations in the data acquisition software system of the multi-channel analyzer (MCA) only 10 ROIs could be simultaneously stored. The stored ROIs are listed in Table 3.1. Note that with the electronics and software available for this experiment this step is essential prior to any tomographic measurements since it provides characteristic information about the trace elements in the fuel shell. With a more advanced system, however, entire spectrum can be collected at each projection condition and then fitted to detect unknown elements in the sample.

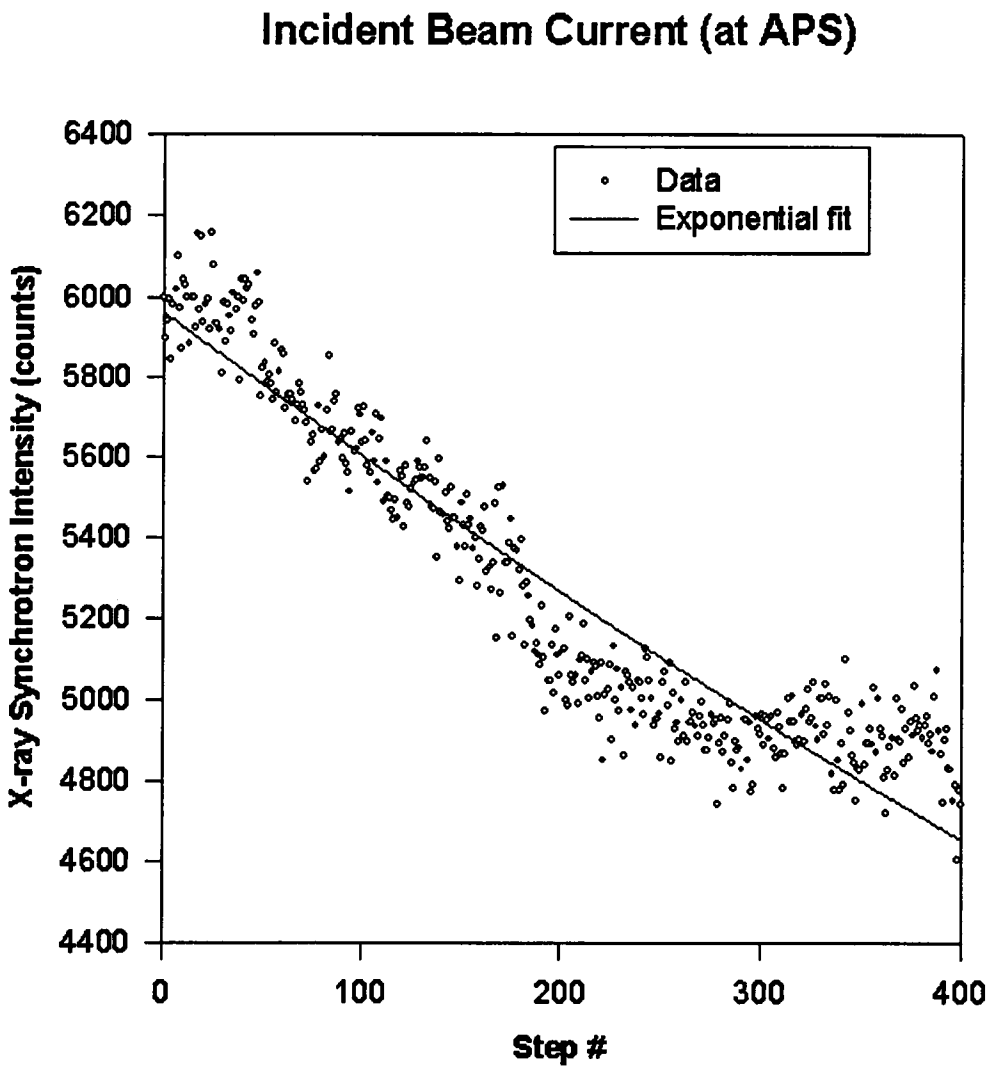

Figure 3.2: Time decay of photon intensity in the APS 2-ID beamline during the tomography experiment.

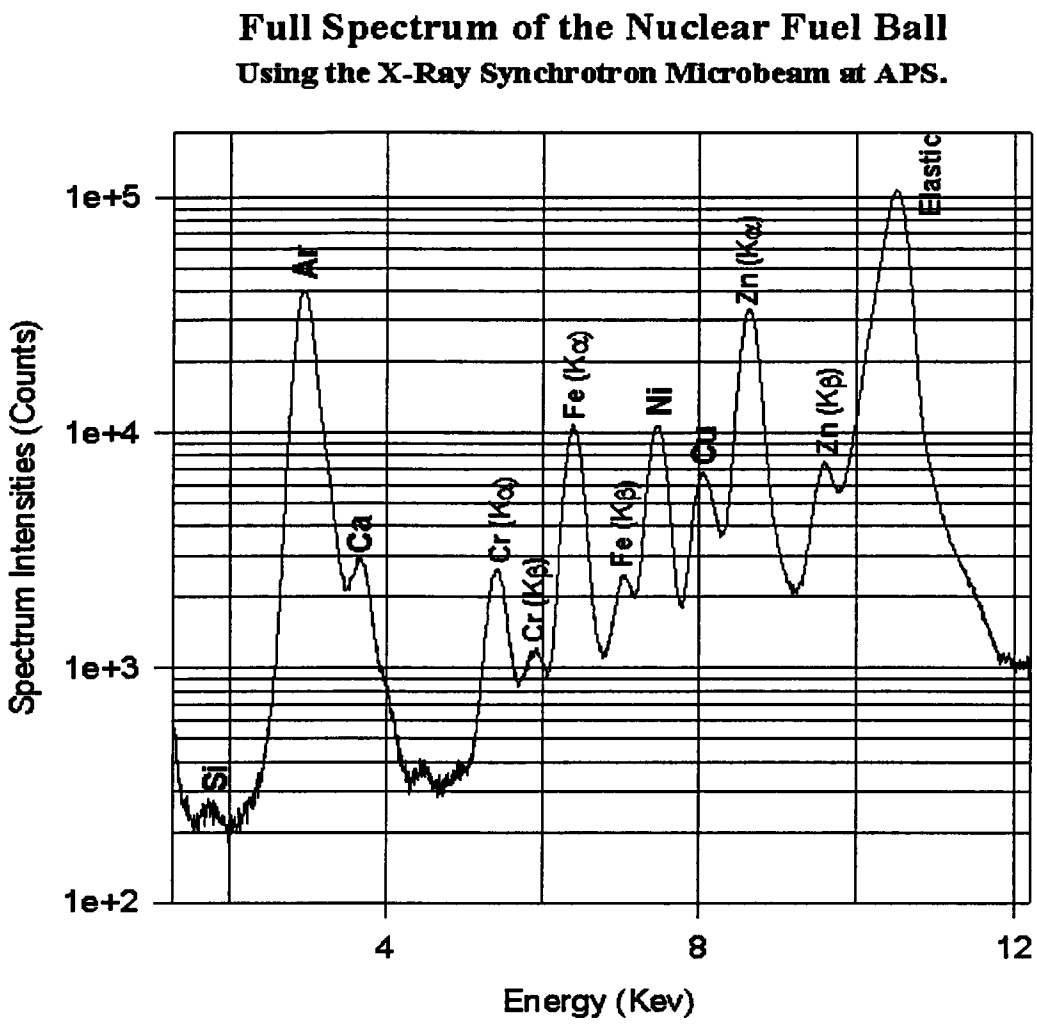

Figure 3.3: Measured fluorescence spectrum from an unfocused beam on the SiC fuel ball shell.

Table 3.1: Measured regions of interest (ROIs) in the fuel ball spectrum.

ROI	**Element**	**MCA Channel Number**		**Energy (keV)**
		Low	High	Center
1	Ar	248	289	2.943
2	Ca	398	475	3.68
3	Ba (lα)	656	698	4.48
4	Cr (kα)	780	845	5.41
5	Cr (kβ)	862	908	5.91
6	Fe	927	1000	6.39
7	Ni	1094	1160	7.482
8	Cu	1179	1242	8.046
9	Zn	1261	1343	8.637
10	Scattering	1556	1617	10.502

In the second phase, a single line scan with 2 μm step size and a MCA livetime of 5 sec was made. The purpose of this experiment was to test the data collection software and hardware and to estimate typical feature sizes. For example, the measured linescan intensities of Zn, Cu, Fe, and Cr are shown in Fig. 3.4. As can be seen, there are numerous small features through the shell, some of which are smaller than the 2 μm step resolution The origin of these trace elements and the mechanisms which led to their inhomogeneous distributions is still subject to speculation.

In the third phase, the tomographic measurements were made for each region of interest. The measurements were compromised by both limitations of the equipment and by limited counting time. For example, the stepping rate of the sample stage and the counting chain response time imposed an overhead of about 2 seconds for each measurement step. Because of the limited beam time availability, a compromised data collection scheme with 8 μm translation steps (101 translation steps), 3° rotation steps (101 rotational steps), and 2 sec MCA livetime was used. This step size was much larger than the probe beam size which later complicated the data analysis. In addition, ~60° of rotation was inaccessible due to the design of the rotation stage. The experiment produced 101 sets of fluorescence projection data which were later used to reconstruct the spatial distribution images of the trace elements. The experimental analysis of the tomographic data is presented in Chapter 4.

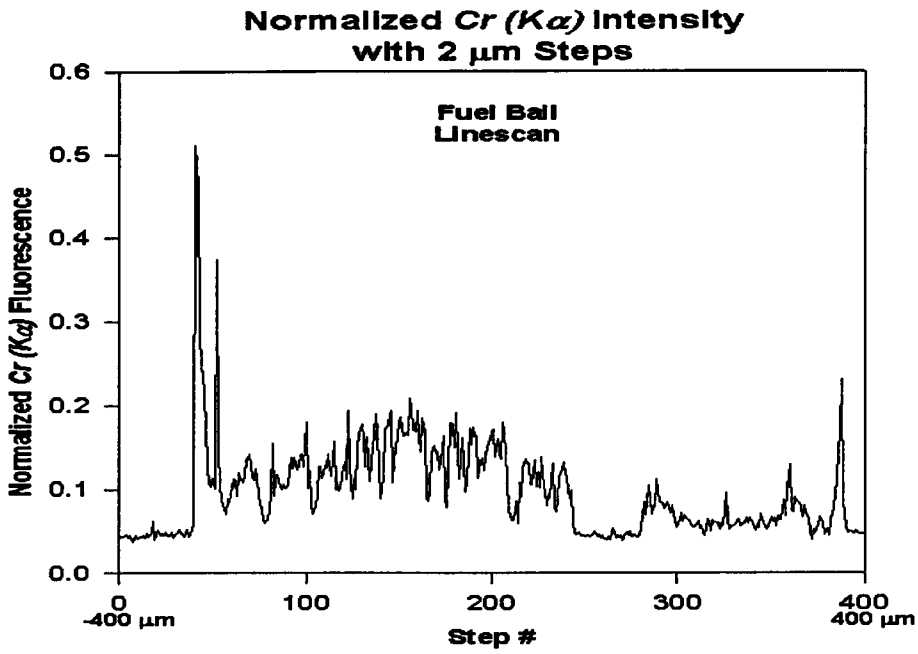

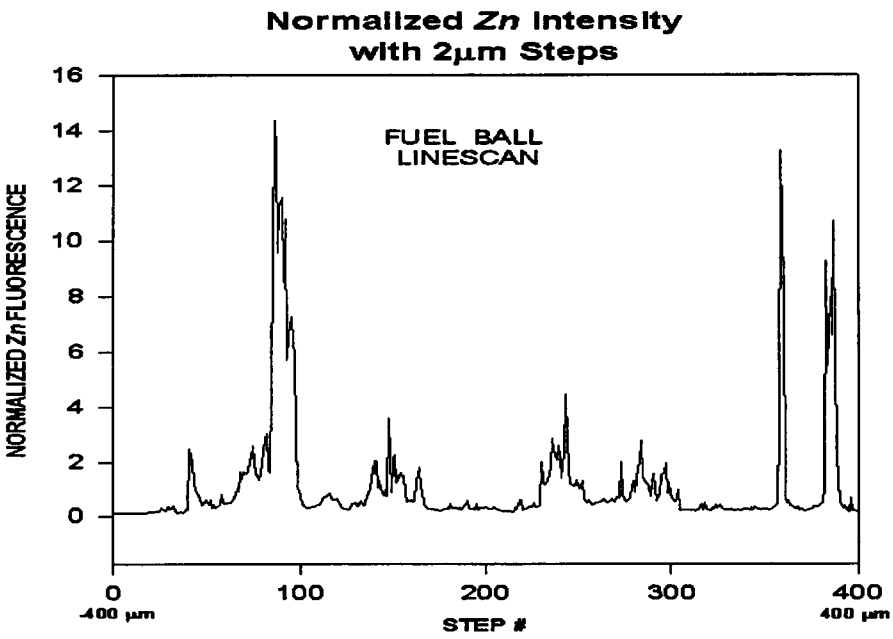

Figure 3.4: Measured fluorescence intensities of trace elements in a linescan experiment on TRISO fuel particle.

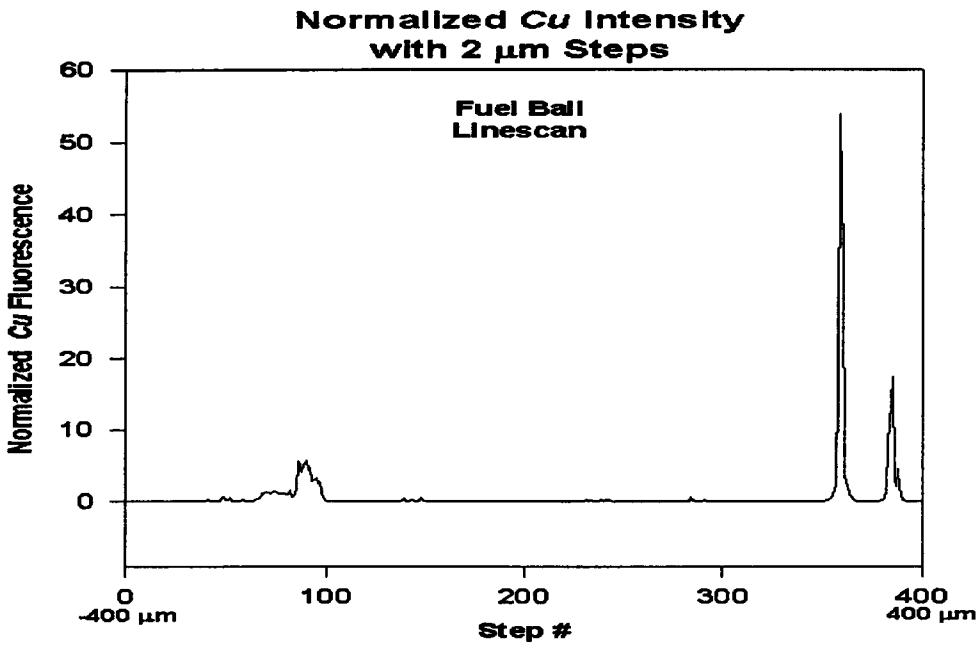

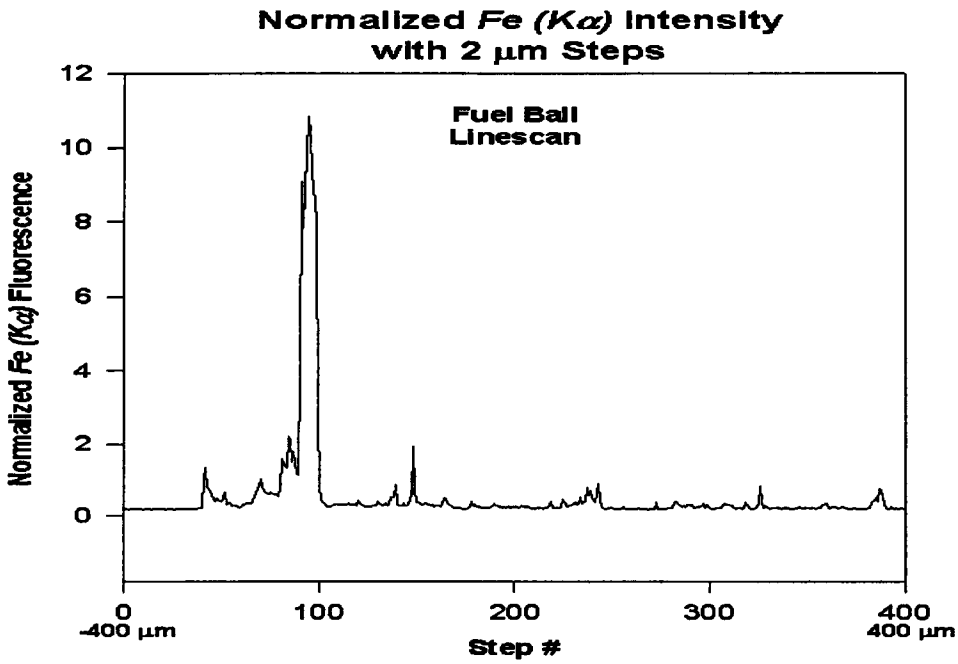

Figure 3.4 (continued)

CHAPTER 4

RESULTS AND EXPERIMENTAL ANALYSIS

4.1 Preprocessing and Analysis of Projection Data

To analyze the tomographic data, it was first necessary to preprocess the projection data. Since the data acquisition software in the tomography experiment stored each projection data set in a separate data file, a computer code written in FORTRAN language was developed to combine the data into a single file. The code reads each data file, removes the comments, and combines all the data sets into a single data file by the name of "tomogarf.dat". It also generates a second data file in which the projection data are normalized to the incident beam intensity and symmetrized with respect to the center of rotation by removing the unwanted data in the Kapton tape. This file was later used for the image reconstruction of the elemental distribution. The file structure for both data files includes 13 columns of data. Columns one and two refer to the translation and angular positions, receptively; columns 3 to 12 correspond to the ROI intensities of 10 measured projection data, and the last column is the MCA realtime. Each column of data includes approximately 10,000 data values.

The data file "Tomograf.dat" was input to a 2-D plotting software to obtain tomographic maps of the measured ROIs. Figure 4.1 shows the plots of the ROI intensities as a

function of angle and position. These raw images reveal a surprising amount of information about the sample. Attention to the correlated patterns in the various ROIs is also required to obtain a meaningful reconstruction of the elemental distributions. For example, the signwave patterns observed in the images of Fig. 4.1 are typical of point inhomogeneities. The inspection of images indicates that the number of inhomogeneities varies with the ROI. In addition as seen in Fig. 4.1, the signwave patterns are not always continuous. This behavior results because the step size used was larger than the convolution of the size of the x-ray probe and the inhomogenities.

Another feature seen in Fig. 4.1, is a marked intensity change in all the images at $\theta \sim 0°$ and 190°. This artifact arises due to scatter from the kapton tape used to encapsulate the sample. Over a small angular range, the kapton tape was at near glancing angle which deflected and absorbed the incident beam. These conditions produced large artifacts in the data which were removed by excluding the data points from a small angular range and averaging neighboring data points to estimate the fluorescence intensities in the missing region. Of the 10^4 data points for each ROI, ~25 were corrected for the effect of the kapton film.

In addition to the kapton artifact, during the measurements, the detector was occasionally saturated by a huge fluorescence signal from an abnormally high concentration of one or more trace elements. Under these conditions, the ROIs from all the elements were

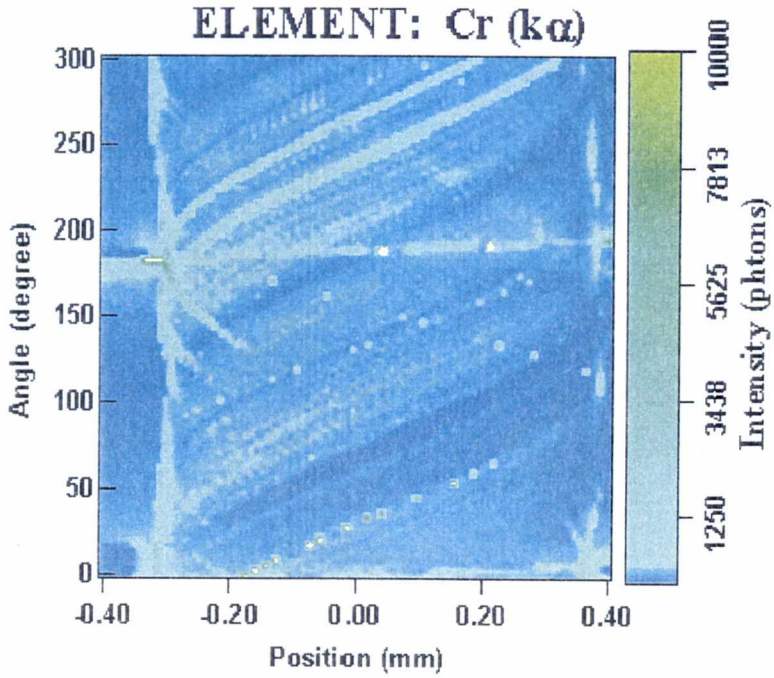

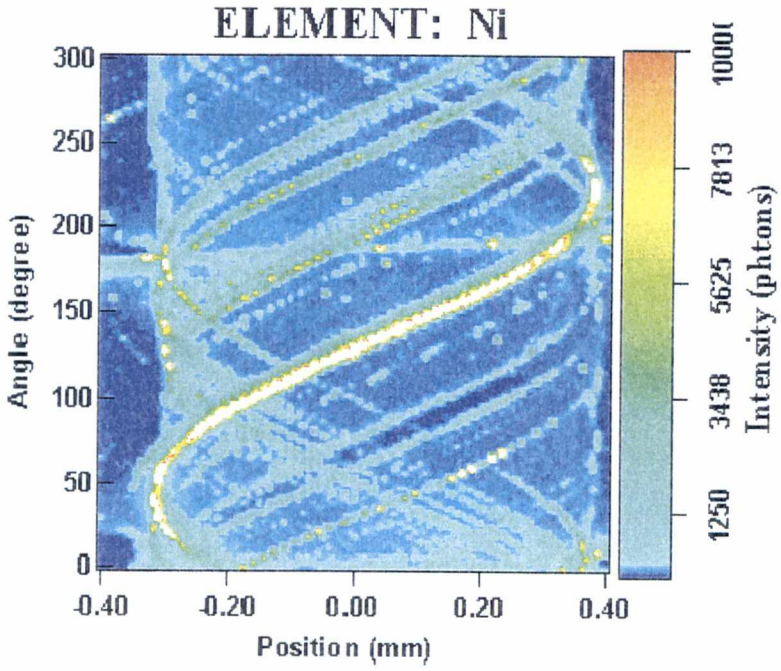

Figure 4.1: Plots of tomographic data of the monitored regions-of-interests (ROIs) in a TRISO nuclear fuel ball.

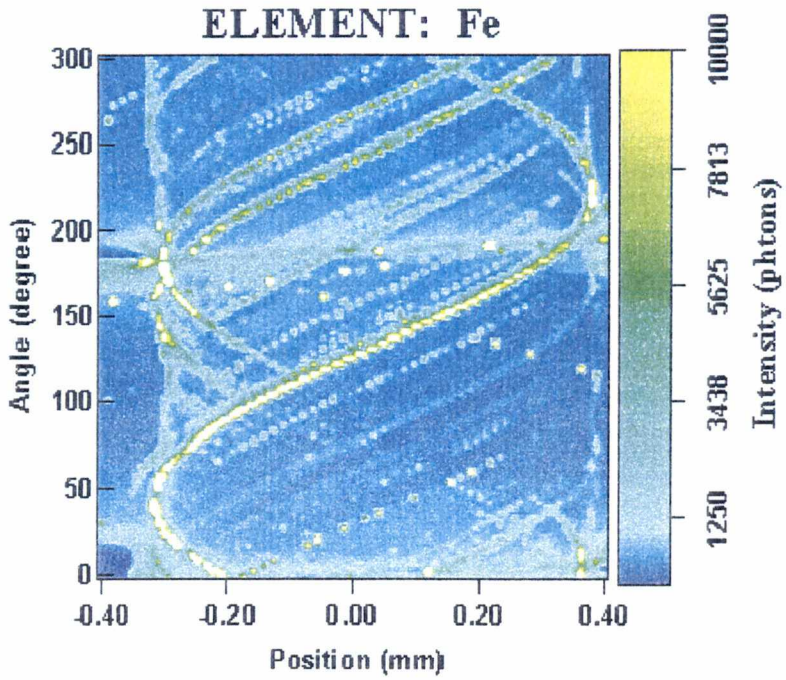

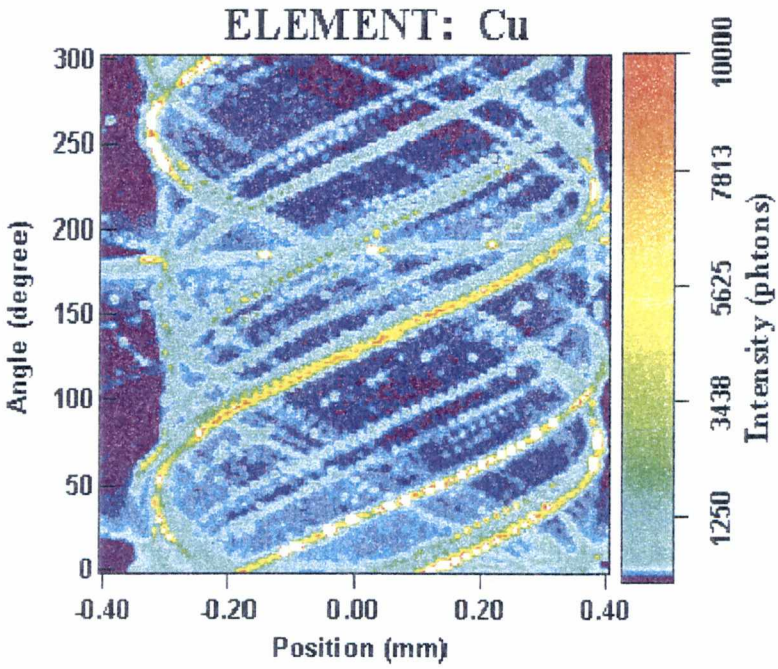

Figure 4.1 (continued)

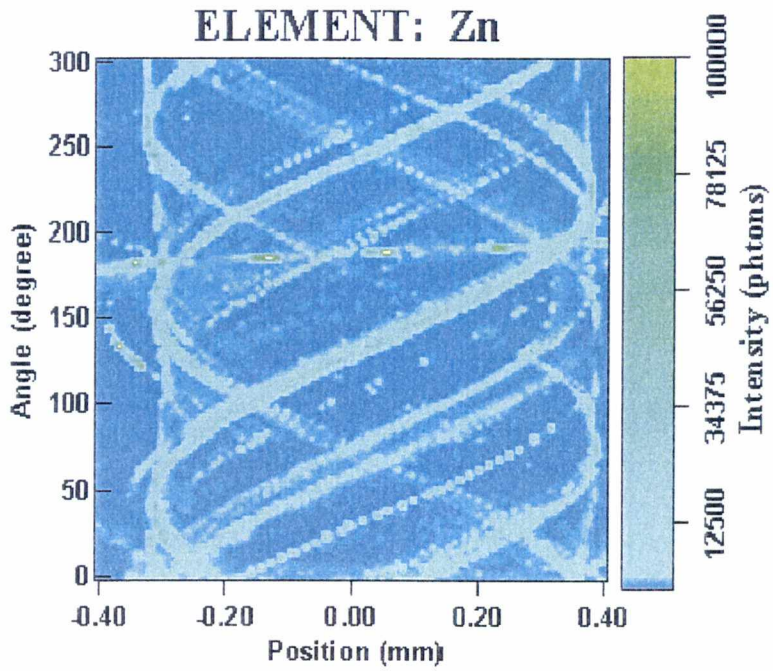

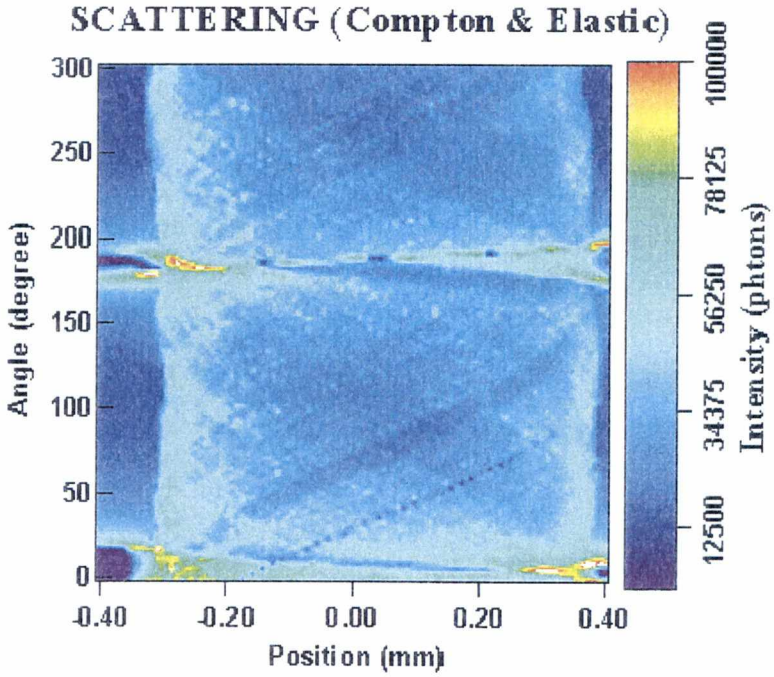

Figure 4.1 (continued)

effected. The elements responsible were identified by observing the angle/translation pattern of each element and comparing them to the intense signal position. Approximately 20 points for each ROI were corrected for saturation effects using average neighboring data points.

4.2 Image Reconstruction Procedure

A computer code written in FORTRAN language was developed to carry out the tomographic reconstructions both with and without absorption correction. The code utilizes the image reconstruction routines from the library suite RECLBL [19] to perform tomographic image reconstruction. The library includes various image reconstruction and projection routines that can be easily adopted into a FORTRAN code. From the RECLBL library, five image reconstruction routines shown in Appendix C were utilized in the computer program.

The front-end of the code was written in Visual Basic. It provides a user friendly interface to input data and information to the program. Drop menus and clicking buttons enable the user to conveniently input a desired reconstruction routine, a frequency filter, a ROI projection data set, and various reconstruction parameters to the program. The program outputs a file containing image reconstruction data of a given ROI. The data can be later used in a commercial graphic software package to obtain a 2-D spatial distribution image of that ROI.

After correcting the artifacts as described in the previous section, the computer code invoked the Fourier filtered backprojection routine of the library to obtain image reconstruction data of each ROI projection data set on a Pentium PC. The mode of reconstruction was based on 360° rotations with no absorption correction and the choice of filter was Hammig with a cutoff frequency of 0.25. As mentioned previously, the stage design limited rotations to ~300° . Because the reconstruction with 360° rotations appeared more robust, the missing 60° data was estimated from the 180° symmetric data.

For the case of absorption correction with a constant attenuation coefficient, the code employs an iterative procedure to estimate the image reconstruction data. In this case, first an approximate reconstruction is obtained using the Grady routine of the library suite [19]. The routine initially assumes no absorption correction to obtain the first approximation. Then, the border searching routine of the library, EVATU, performs a boundary search on the approximated reconstructed image using an object-to-background ratio of 2.5. After identifying the approximated borders, the routine EVATU evaluates the attenuation factors throughout the object. These factors are then sent back to the Grady routine to obtain a new approximate reconstruction which subsequently provides new attenuation factors. The above iteration should continue until the variations in attenuation factors between two subsequent iterations become small.

The attenuation coefficient for SiC was determined for each trace element at its fluorescence energy using the x-ray cross section table [22]. For the elastic and Compton scattering, the coefficient was evaluated at the incident beam energy, 10.5 keV. The

following equation is applied to evaluate the linear attenuation coefficient at a given energy.

$$\mu_{SiC} = \rho_{Si}\sigma_{Si} + \rho_C\sigma_C \tag{4.1}$$

where μ_{SiC} (cm^{-1}) is the linear attenuation of the SiC, and ρ(gr/cm^3) and σ(cm^{-2}/gr) refer to density and cross section of Si and C, respectively. The values of attenuation coefficients for each ROI energy are presented in Table 4.1.

4.3 Estimation of Elemental Concentration

The absolute elemental concentrations were estimated by comparing the observed fluorescence signal to x-ray elastic and Compton scattering intensities. The total scattering cross section of SiC at 90° was evaluated from reference [23]. The incident beam polarization factor was estimated at ~5% and multiple scattering and absorption were assumed to be small. With these approximation, the factor $I_o\Omega$ was determined, where I_o is the incident beam flux intensity in photons/sec/μm^2 and Ω is the detector solid angle. With the assumption of negligible absorption, the trace element concentration were then estimated using Equation (2.5). The approximation of elemental concentration was carried out based on the following steps.

1. Determined number of atoms of Si and C in one cm^3

$$N_{si} = N_c = N_{SiC} = \frac{\rho_{SiC} \times 6.023 \times 10^{23}}{Atomic\,Weight_{SiC}} \tag{4.2}$$

where N refers to number of atoms in one cm^3, $\rho_{SiC} = 3.22$ (g/cm^3) is the density of SiC,

Table 4.1: Linear absorption coefficients of SiC at measured ROI energies.

Energy (keV)	**C cross section (cm^2/g)**	**Si cross section (cm^2/g)**	**Calculated linear attenuation coefficient of SiC (1/cm)**
2.943	1.022578×10^{2}	1.09496×10^{3}	2.55089×10^{3}
3.680	5.43352×10^{1}	6.36236×10^{2}	1.47731×10^{3}
5.410	1.52372×10^{1}	2.10185×10^{2}	4.85435×10^{2}
5.910	1.11972×10^{1}	1.60935×10^{2}	3.71243×10^{2}
6.390	9.26390	1.34363×10^{2}	3.09860×10^{2}
7.482	5.88600	8.90660×10^{1}	2.05154×10^{2}
8.046	4.25000	6.60000×10^{1}	1.51920×10^{2}
8.637	3.61837	5.61700	1.29294×10^{2}
10.502	2.04450	3.20040×10^{1}	7.36384×10^{1}

and the *Atomic Weight*$_{SiC}$ = 40.1 (*gr SiC/gr atom SiC*). Thus, using the above equation gives $N_{Si} = N_C = N_{SiC} = 4.836\times10^{22}$ (atoms/cm^3).

2. Estimated elastic and Compton scattering and volume of SiC shell confined within the incident x-ray beam dimensions.

$$\sigma = \sigma_{elastic} + \sigma_{Compton}$$
$$\sigma_{Si} = (5.31 + 8.79)\times 7.94\times10^{-26} = 1.12\times10^{-24}\ (cm^2) \qquad (4.3)$$
$$\sigma_C = (1.54 + 4.672)\times 7.94\times10^{-26} = 0.4932\times10^{-24}\ (cm^2)$$

The volume is the product of the beam dimensions by the thickness of the SiC shell. The beam dimensions are 1μm × 3μm and the estimated thickness for SiC shell is 38 μm. Thus, the estimated SiC volume is $1\times3\times(2\times38)\times10^{-12}=2.28\times10^{-10}$ (cm^3).

3. Estimated the $I_o\Omega$ from the elastic and Compton scattering data using the following equation.

$$I = I_o\Omega(N_{Si}\sigma_{Si} + N_C\sigma_C)V \qquad (4.4)$$

where V is the estimated SiC volume in the Step 2 and I is the measured elastic and Compton scattering intensity . Substituting the values calculated in Steps 1 and 2 into Eq. (4.4) gives the following relationship between I and $I_o\Omega$.

$$I_o\Omega = 5.622\times10^{10} I \qquad (4.5)$$

At the projection angle θ=0 and at the centerline of the SiC shell where the incident beam is positioned, the measured I is 60456 (photons/sec) and the determined $I_0\Omega$ from Equation (4.5) is 3.4×10^{15} (photons/sec cm^2). Since the polarization factor is ~5%, the calculated value for the $I_o\Omega$ should be multiplied by 20 to obtain a correct estimate of true

$I_o\Omega$ during the experiment (~.6.8×10^{16} photons/sec cm^2). Assuming the detector has a 110 mm^2 area 30 mm from the sample, the value of I_o is 5.5×10^9 photons/s/μm^2 or about 1.5×10^{10} photons/sec in 1×3 μm beam. This number is near a value measured for the beamline using an ion chamber.

4. Determined the trace element concentration according to the following equation.

$$I_F = I_o\Omega(C_T\sigma_T)\omega_K \tag{4.6}$$

where I_F is the measured fluorescence intensity of a trace element, ω_K is the fluorescence yield, and C_T and σ_T refer to concentration and the fluorescence cross section of the trace element, respectively. The fluorescence cross section is determined at the incident beam energy, 10.53 keV. It should be pointed out that concentrations derived as described above are only good for an order of magnitude estimate due to crystal effects on the scattering cross section which are not included in this estimate.

4.4 Analyses of Tomographic Images

The reconstructed spatial distributions of the monitored ROIs are presented in Fig. 4.2 and Fig. 4.3. Figure 4.2 shows the reconstructed distribution without absorption correction and Fig. 4.3 shows the distribution with absorption correction. The images for the elastic and Compton scattering effects in both figures verify that the SiC shell is ~38μm thick. They also indicate that the shell shape of thickness is not uniform. In two different locations the shell thickness reduces to ~8μm. The reconstructed images

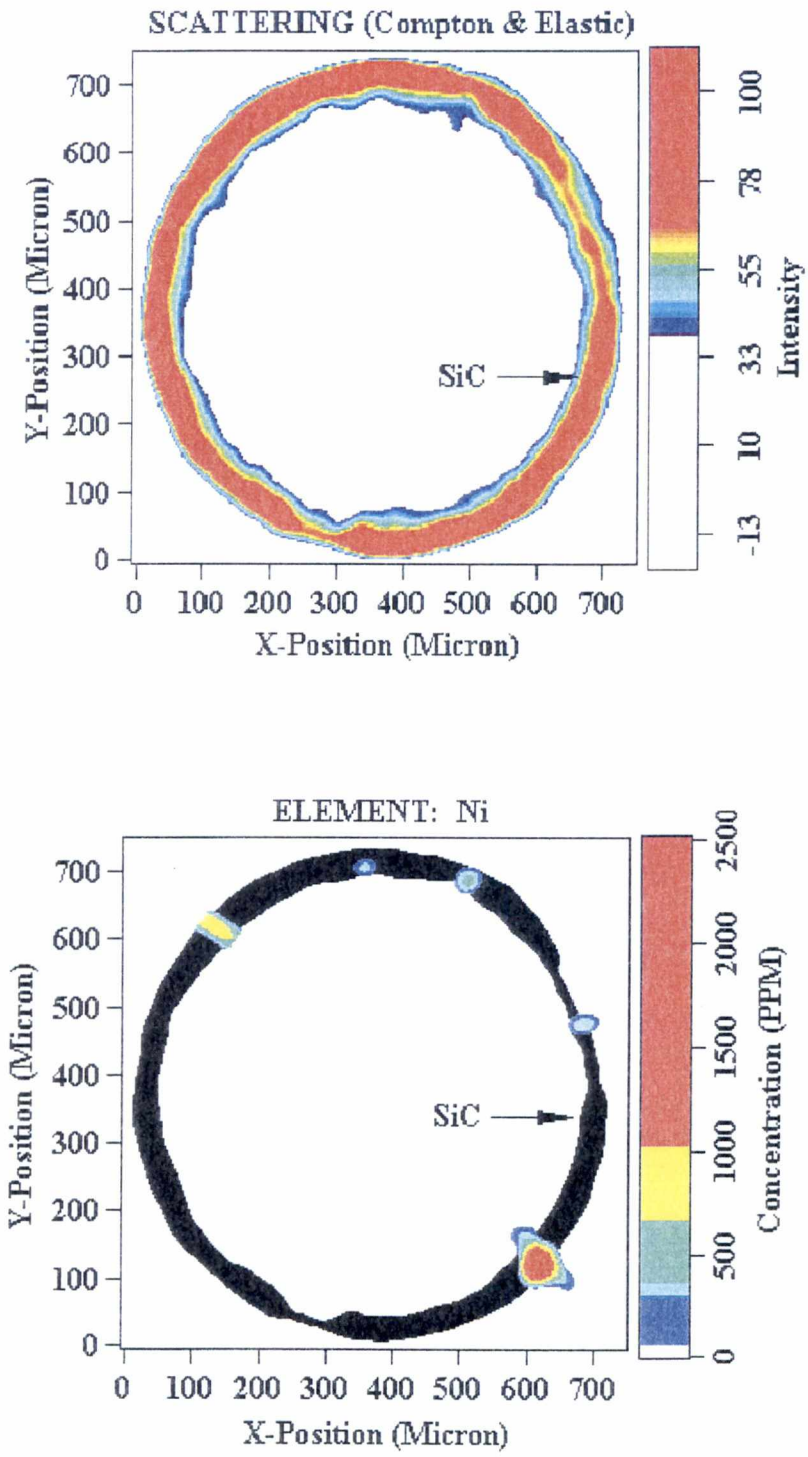

Figure 4.2: Reconstructed images of the spatial distribution of trace elements without absorption correction. The reconstructed elemental distributions are superimposed on the reconstructed shell from the elastic/Compton scattering.

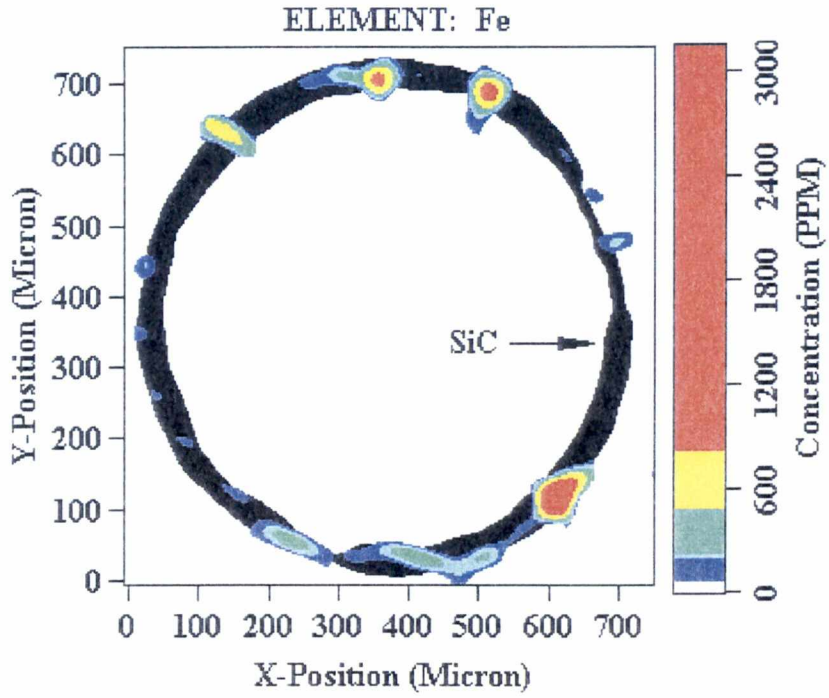

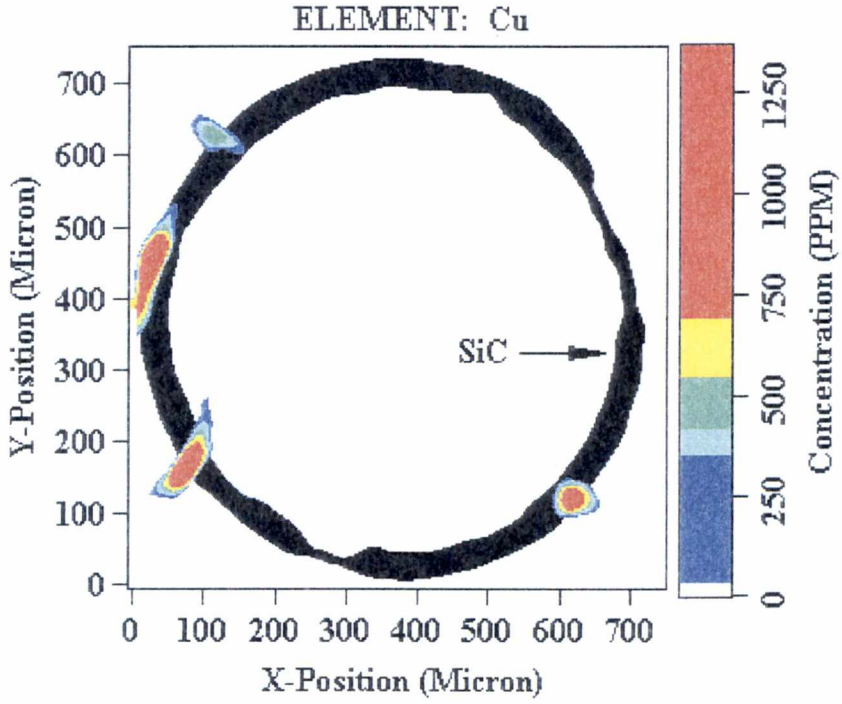

Figure 4.2 (continued)

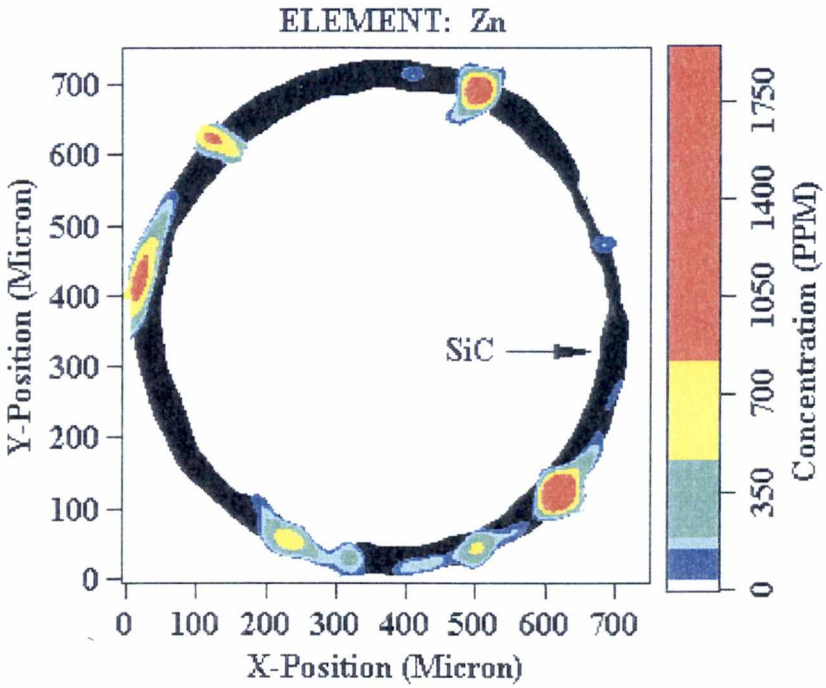

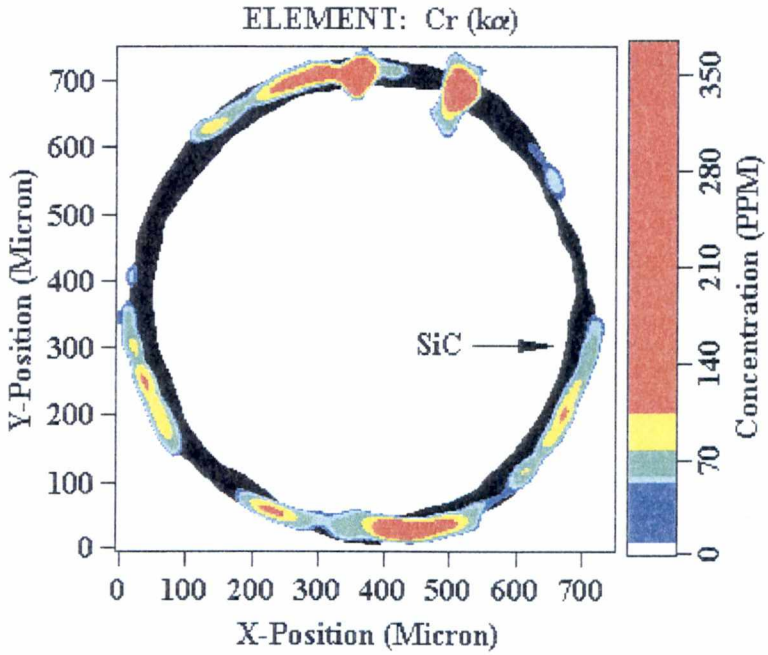

Figure 4.2 (continued)

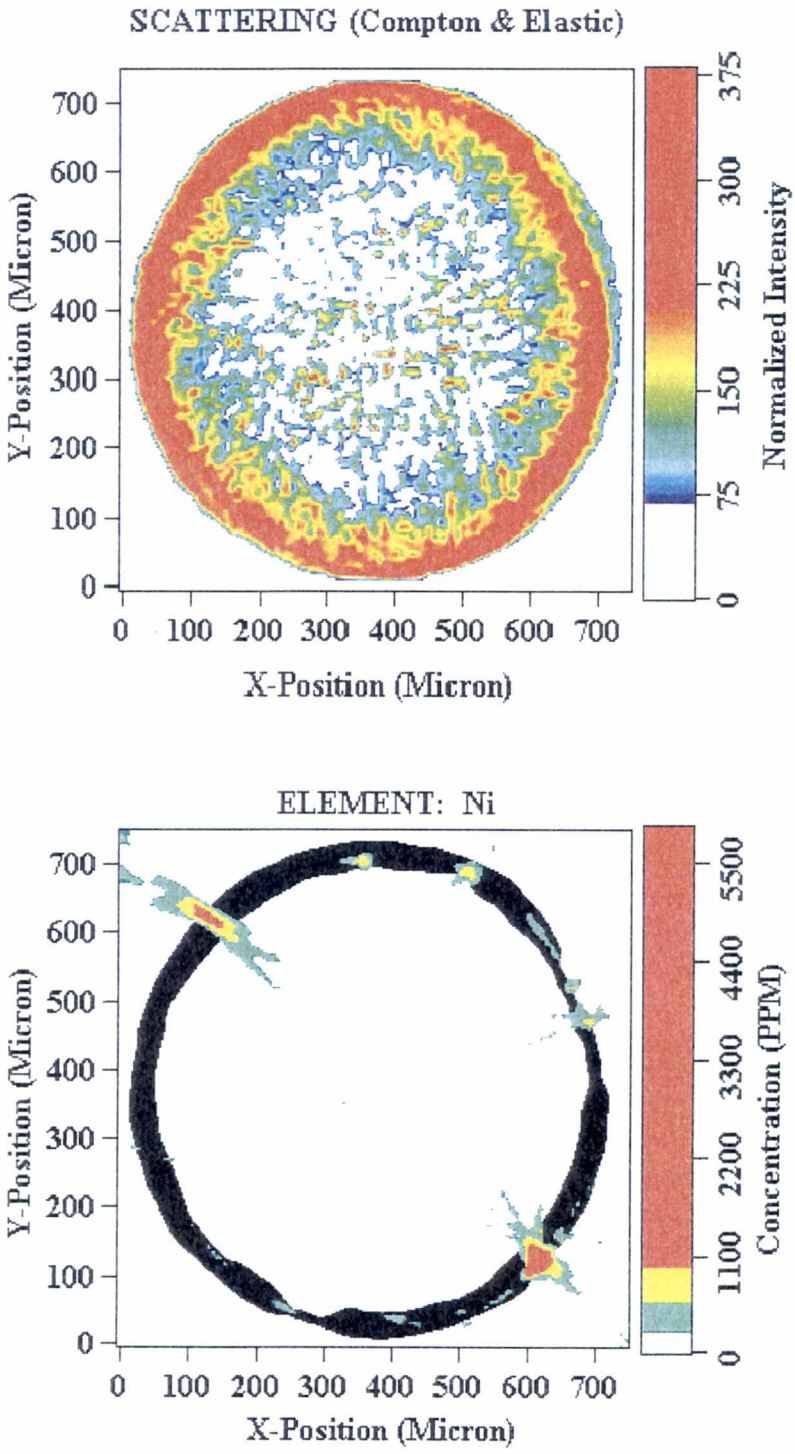

Figure 4.3: Reconstructed images of the spatial distribution of trace elements with absorption correction.

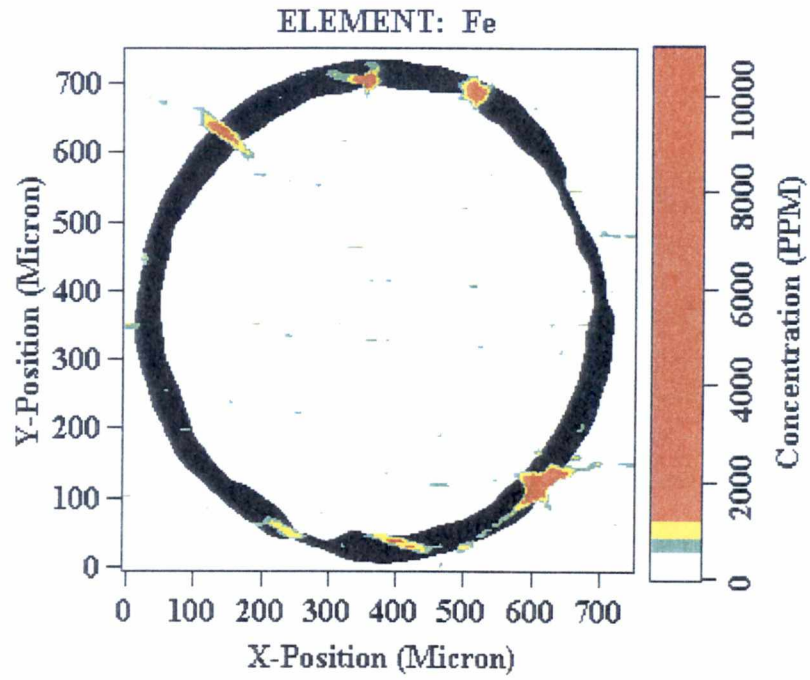

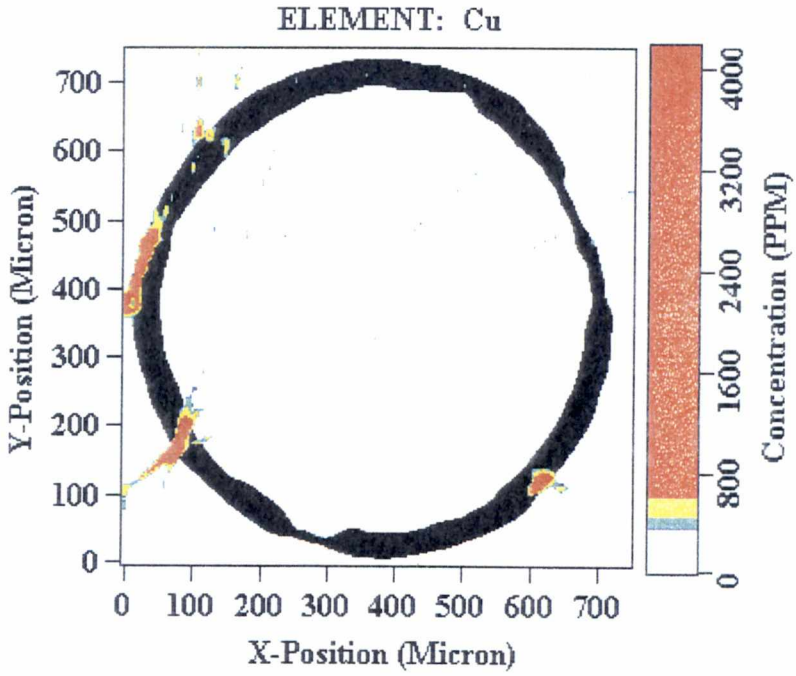

Figure 4.3 (continued)

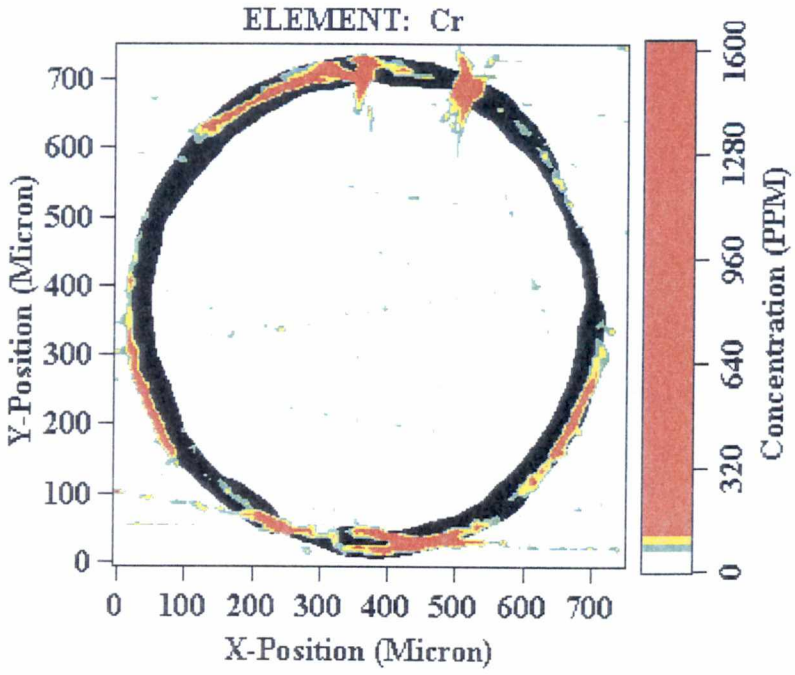

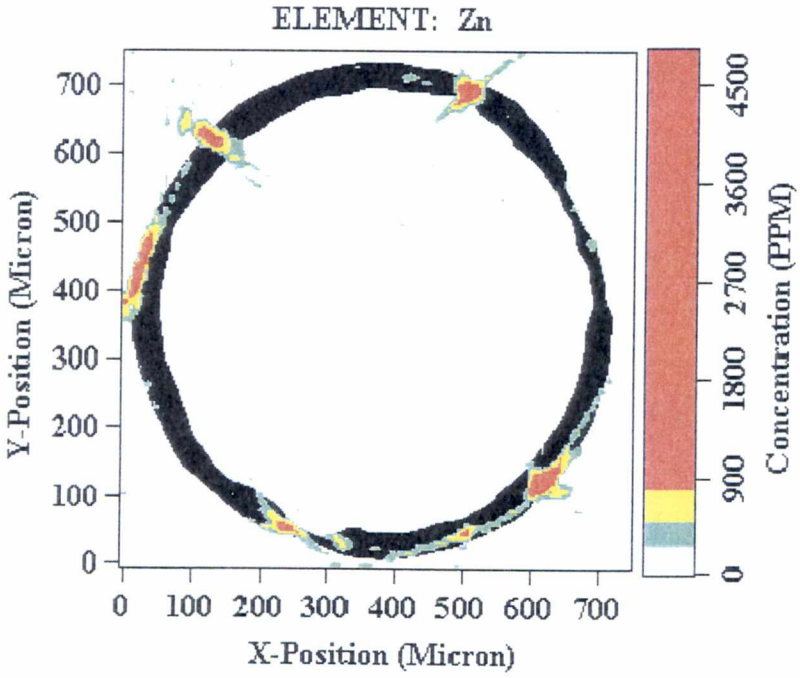

Figure 4.3 (continued)

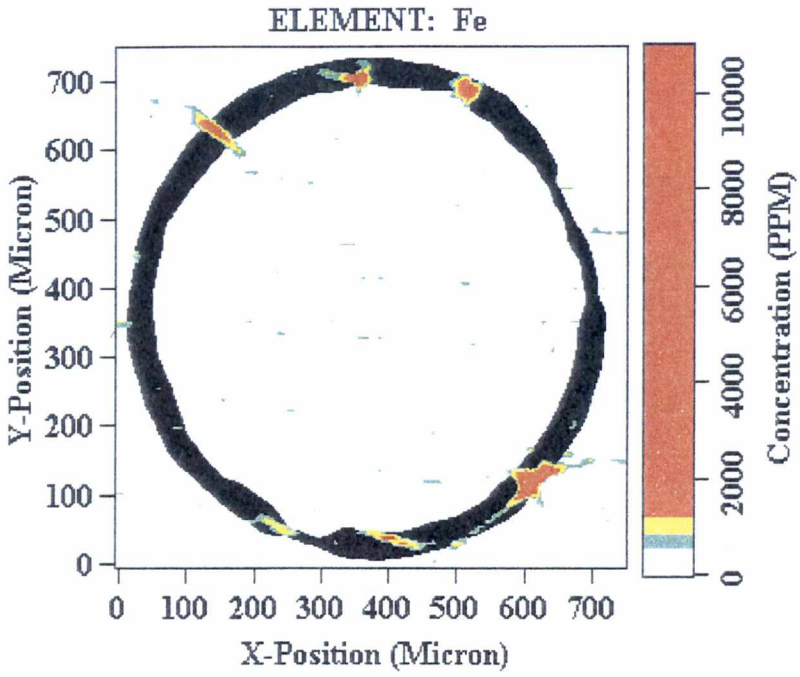

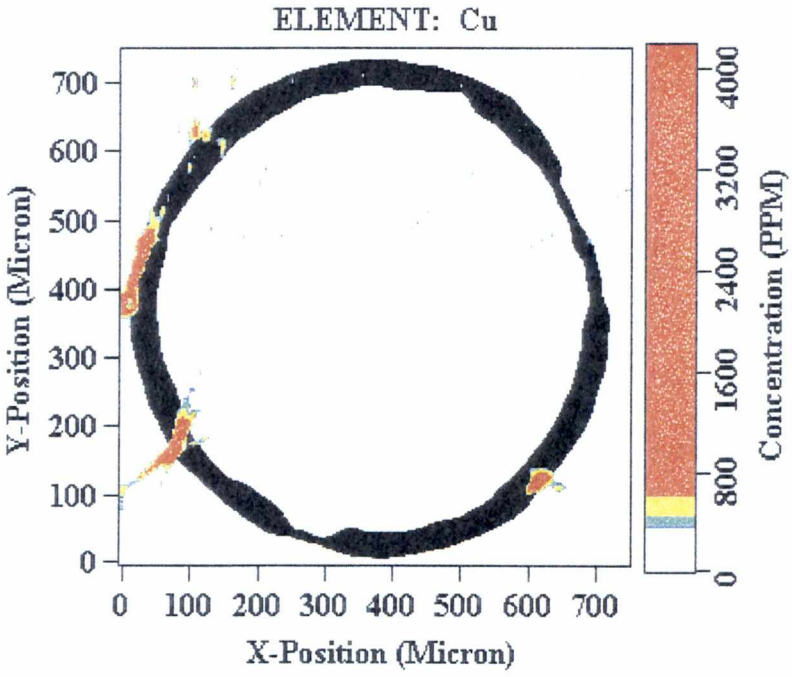

Figure 4.3 (continued)

indicate that the trace elements are spatially distributed predominately at the outer edge of the SiC shell. Only, Cr appears to be spread throughout the SiC shell. As can be seen in the images of both Fig.4.2 and Fig. 4.3, a highly concentrated piece of material exists in the vicinity of x=630 μm and y=110 μm. The constituents of the material appear to be Ni, Fe, Cu, and Zn with more concentrations in Fe and Ni. Though, at the present time, it is not possible to confidently identify the origin of the observed trace elements, they may have been originated from impurities associated with the fuel, SiC, and/or fabrication processes. For example, the SiC shells are deposited in metal chambers. Small impurities from the chamber walls may be introduced into the SiC shell during deposition.

The comparison between the images of Fig. 4.2 and Fig. 4.3 also reveals that the absorption correction can be large even in these very small ~ 38 μm thick samples. This is particularly evident for low energy fluorescence lines. For example, ~97% of Ba fluorescence (4.48 keV) can be absorbed by the SiC shell. As a result, the distributions of trace elements are most easily detected near the surface of the SiC shell. Clearly a higher counting rate is required to improve the signal-to-noise ratio for low energy fluorescence lines.

The images in Fig. 4.3 contain more background noise than those of Fig. 4.2. This is mainly due to the fact that the reconstruction algorithm for the absorption correction is an iterative method and requires a proper value for the object-to-background ratio. The number of iteration is normally compromised with computational cost and/or time and a

proper value for the object-to-background ratio is obtained through an elaborate trial and error procedure. Thus, to improve the quality of the reconstructed images with absorption correction, longer experimental measurement times are required to collect better statistics on a finer mesh.

CHAPTER 5

SUMMARY, CONCLUSIONS, AND RECOMMENDATIONS FOR FUTURE WORKS

5.1 Summary

Nondestructive x-ray fluorescence microtomography was applied to the experimental study of spatial distributions of trace elements in the SiC shell of an advanced nuclear fuel particle, TRISO. As qualitatively compared in Section 2.7, x-ray fluorescence microtomography in general offers a much higher elemental sensitivity than transmission tomography for characterizing high Z trace elements in a low Z matrix. Thus, it is a promising tool to study spatial distributions of trace elements in the SiC shell.

To carry out the study, an experimental setup was designed at beamline 2-ID of the Advanced Photon Source (APS). The setup utilized a monochromatic 10.5 keV x-ray beam, hard x-ray zone plate focusing optics, a precision translation and rotation stage, and a high performance solid state detector to measure fluorescence signals from the SiC shell of the TRISO fuel particle. The fluorescence measurements were recorded by a computerized data acquisition system connected to the experiment instruments.

As detailed in Chapter 3, three fluorescence experiments were performed on the TRISO fuel particle. In the first experiment, the fluorescence spectrum of trace elements in the SiC shell was determined by using an unfocused x-ray beam on the fuel particle. The analysis of the spectrum indicated the presence of trace elements Fe, Cu, Cr, Ni, and Ba in the SiC shell. In addition, the spectrum was used to select ten important ROIs for both fluorescence linescan and tomographic measurements. In the second experiment, a linescan with 2 μm resolution was made to obtain typical feature sizes of trace elements in the SiC shell. In the third experiment, tomographic measurements were made for all 10 ROIs using a beam size of 1 μm by 3 μm. However, the data collection scheme was set with 8 μm translation steps (101 translation steps) and 3° rotation steps (101 rotational steps). This resulted in 101 sets of projection data for each ROI.

The sinogram of tomographic data for each ROI was plotted and then analyzed for artifacts. The artifacts because of kapton film effects and detector saturation were identified and replaced with average values of neighboring data points. The initial analysis of trace element sinograms indicated that the monitored trace elements were approximately located near the outer edge of the SiC shell.

After correcting the artifacts, a computer code written in FORTRAN language utilized the backprojection of filtered projection algorithm, to perform tomographic image reconstructions for the monitored ROIs. The tomographic reconstructions were carried out both with and without absorption correction. The reconstructed images revealed that the SiC shell was ~38 μm thick and the trace elements had localized spatial distributions

near the outer edge of the shell. The results and analysis of tomographic images were presented and discussed in Chapter 4.

5.2 Conclusions

X-ray fluorescence microtomography is an emerging technique made practical by high brilliance x-ray sources, advanced x-ray focusing optics and high-performance x-ray detectors. This thesis demonstrated that the fluorescence microtomography technique can be a powerful tool for investigating elemental distributions in materials. The technique is nondestructive and noninvasive with a high spatial resolution. It is sensitive to high Z trace elements in a low Z matrix with PPM accuracy, and has a good signal-to-noise ratio. Fluorescence microtomography can be used to simultaneously identify the elemental distributions of many trace elements. With rapid advances in x-ray optics, the technique of microtomography promises to have a major impact on characterization, design, development, and understanding of advanced materials.

The results of this research show that fluorescence signals from elements with low energy fluorescence lines can be significantly attenuated in the sample's medium which introduces large uncertainties in correct and accurate identification and estimation of such elements. This problem can be greatly alleviated by improving the photon counting statistics, by using multiple detectors, and by implementing a more powerful reconstruction algorithm with more advanced absorption correction features.

The main drawbacks of fluorescence microtomography are limited access to high intense synchrotron sources and the slow data collection rate . The results of this experimental study point to several ways to accelerate data collection. For example, with a broad-bandpass monochromator, the fluorescence signal can be increased by 2-3 orders of magnitude with no loss in spatial resolution or signal-to-noise. With such an intense probe, it will be necessary to use wavelength dispersive spectrometers with integrating rather than single photon detectors. Such an arrangement will simultaneously increase spatial resolution and will greatly increase the sensitivity for minor trace elements of interest.

It should also be noted that in our experiment the beam energy was much lower than the K absorption edges of heavy elements such as Cs, Ce, Eu, and Ru. We therefore could not excite the K lines of these elements; the L lines are masked by overlapping K lines of less interesting trace elements. To positively measure the elemental distribution of Cs for example, either a crystal spectrometer or a high energy (>36 keV) x-ray probe are required.

5.3 Recommendations for Future Works

The experimental study conducted in this thesis was mainly focused on a 2-D spatial distributions of trace elements through the SiC shell of an advanced TRISO fuel particle. An obvious extension of the work is to experimentally investigate the trace element distributions in 3-D. Currently, there are no such studies are available for advanced nuclear fuel particles. The experimental setup and procedures for this investigation are

similar to those described in this work. In fact, it is only necessary to repeat the fluorescence microtomography experiment performed in this study at pre-specified intervals in a direction perpendicular to the 2-D planes of elemental distributions. To efficiently perform such an experiment, the data collection rate should be significantly increased as elaborated in the previous section.

Another interesting problem would be to confidently verify the sensitivity of fluorescence microtomography for high Z trace elements in a low Z matrix. For example, the elemental loading of the fuel cell is known for radioactive isotopes. This makes these samples ideal for evaluating the overall sensitivity of fluorescence microtomography experiments in such samples. In addition, the sensitivity evaluation can be examined with other type of samples. For example, National Bureau of Standards has standard samples with known concentrations and distributions of trace elements. These samples can be used in fluorescence microtomography experiments to measure elemental concentrations and distributions. A comparison between measured and true values can show the accuracy and sensitivity of the experiments.

REFERENCES

REFERENCES

[1] B. P. Flannery and W.G. Roberge, "Observation Strategies for Three-Dimensional Synchrotron Microtomography," J. Applied Physics, vol. 62, no. 12, Dec. 1987, pp. 4668-4674.

[2] B. P. Flannery, H. W. Deckman, and W. G. Roberge, "Three-Dimensional X-ray Microtomography," Science, vol. 237, Sept. 1987, pp. 1439-1444.

[3] G. E. Ice, "Microbeam-Forming Methods for Synchrotron Radiation," X-ray Spectrometry, Vol. 26, pp. 315-326, 1997.

[4] B.F. Myers, F.C. Montgomery and K.E. Partain, "The Transport of Fission Products in SiC," Doc No. 909055, GA Technologies Inc., 1986.

[5] P. Krautwasser, G. M. Begun, and Peter Angelini, *J. of American Ceramic Society*, **66** 424, 1983.

[6] See for example, Q.C. Johnson, J.H. Kinney, U. Bonse and M.C. Nichols, *Proc. Mater. Soc. Symp.*, **69**, 203, 1986.

[7] J.H. Kinney and M.C. Nichols, *Annu. Rev. Mater. Sci.*, **22** 121, 1992.

[8] "Proceedings of the Workshop on High Resolution Computed Microtomography (CMT)," Lawrence Berkeley National Laboratory , U. of California, August 12-13, 1996.

[9] Paul Boisseau, "Determination of Three Dimensional Trace Element Distributions by the Use of Monochromatic X-Ray Microbeams", Ph.D. Dissertation, MIT, 1986.

[10] C.J. Sparks, "X-ray Fluorescence Microprobe for Chemical Analysis", pg 459-512 in Synchrotron Radiation Research, edited by H. Winick and S. Doniach Plenum Press, New York, 1980.

[11] Katsuhisa Usami and Tatsumi Hirano, "X-ray Microtomography," Application of Synchrotron Radiation to Materials Analysis edited by H. Saisho and Y. Gohshi," Elsevier Science, 1996.

[12] A. Snigirev, "Bragg-Fresnel Optics: New Field of Application, Proceedings of the Workshop on High Resolution Computed Microtomography (CMT), Lawrence Berkeley National Laboratory , U. of California, August 12-13, 1996.

[13] "Proceedings of the Sixth Users Meeting for the Advanced Photon Source," ANL/APS/CP-6, Argonne National Laboratory, May 25-26, 1994.

[14] "ALS Handbook, a Summary of the Capabilities and Characteristics of the Advanced Light Source," Lawrence Berkeley Laboratory, PUB-643 Rev.2, April 1989.

[15] G. E. Ice personal communications.

[16] M. Terasawa and M. Kihara, "Basic Characteristics of synchrotron radiation and its related facilities and instrumentation," Application of Synchrotron Radiation to Materials Analysis edited by H. Saisho and Y. Gohshi," Elsevier Science, 1996.

[17] G. T. Herman (editor) "Image Reconstruction from Projections: Implementation and Applications," Springer-Verlag, Berlin, 1979

[18] G.T. Herman, "Image Reconstruction from Projections: The Fundamentals of Computerized Tomography," Academic Press, New York, 1980.

[19] R. H. Huesman, G.T. Gullberg, W.L. Greenberg, T. F. Budinger, "RECLBL Library Users Manual, Donner Algorithms for Reconstruction Tomography," Pub. 214 Lawrence Berkeley Laboratory, U. of California, 1977.

[20] Lioyd D. Fosdick, E. R. Jessup, C. J. C. Schauble, and G. Domik, "An Introduction to High-Performance Scientific Computing," MIT Press, Massachusetts, 1996.

[21] Azriel Rosenfeld and Avinash C. Kak, "Digital Picture Processing," Academic Press, New York, 1976.

[22] "Operating Manual XR-100T, X-Ray Detector System and PX2T Power Supply/Shaper," AMPTEK Inc., MA, U.S.A, June 1996.

[23] M. O. Krause,C.W. Nestor, Jr., C. J. Sparks, Jr., E. Ricci, "X-ray Fluorescence Cross Sections for K and L Rays of the Elements," Oak Ridge National Lab. Tech. Report ORNL-5399, 1978.

[24] Gerald R. Lachance and Fernand Claisse, "Quantitative X-ray Fluorescence Analysis, Theory and Application," John Wiley and Sons, New York, 1995.

[25] W. Yun, B. Lai, D. Shu, A. Kounsary, Z. Cai, J. Barraza, D. Legnini, "Design of a Dedicated Beamline for X-ray Microfocusing and Coherence Based Techniques at the Advanced Photon Source"

APPENDICES

APPENDIX A

SYNCHROTRON RADIATION AND BEAMLINE 2-ID AT THE ADVANCED PHOTON SOURCE

This appendix presents an overview of synchrotron radiation and a brief description of beam line 2-ID at advanced photon source (APS). References [11,14,25] are used to extract information for this appendix, and they should be consulted for more details.

A.1 Synchrotron Radiation

Synchrotron radiation refers to the electromagnetic radiation emitted by relativistic particles when accelerated transverse to their path by a magnetic field. Modern synchrotron radiation sources rely on "storage rings" which store electron or positron bunches along circular orbits (see Fig. A.1). The storage ring includes an array of bending magnets and a number of straight linear sections. The bending magnets are used to bend and focus the electron beam during the acceleration phase in order to maintain the electron bunches in the same orbital path. The linear sections contain undulators or wigglers known as insertion devices which accelerate the electrons perpendicular to the main velocity and produce the most intense synchrotron radiation.

Synchrotron radiation offers major advantages for both soft and hard x-ray applications as compared to conventional x-ray sources. These advantages, as stated in the reference [11], include

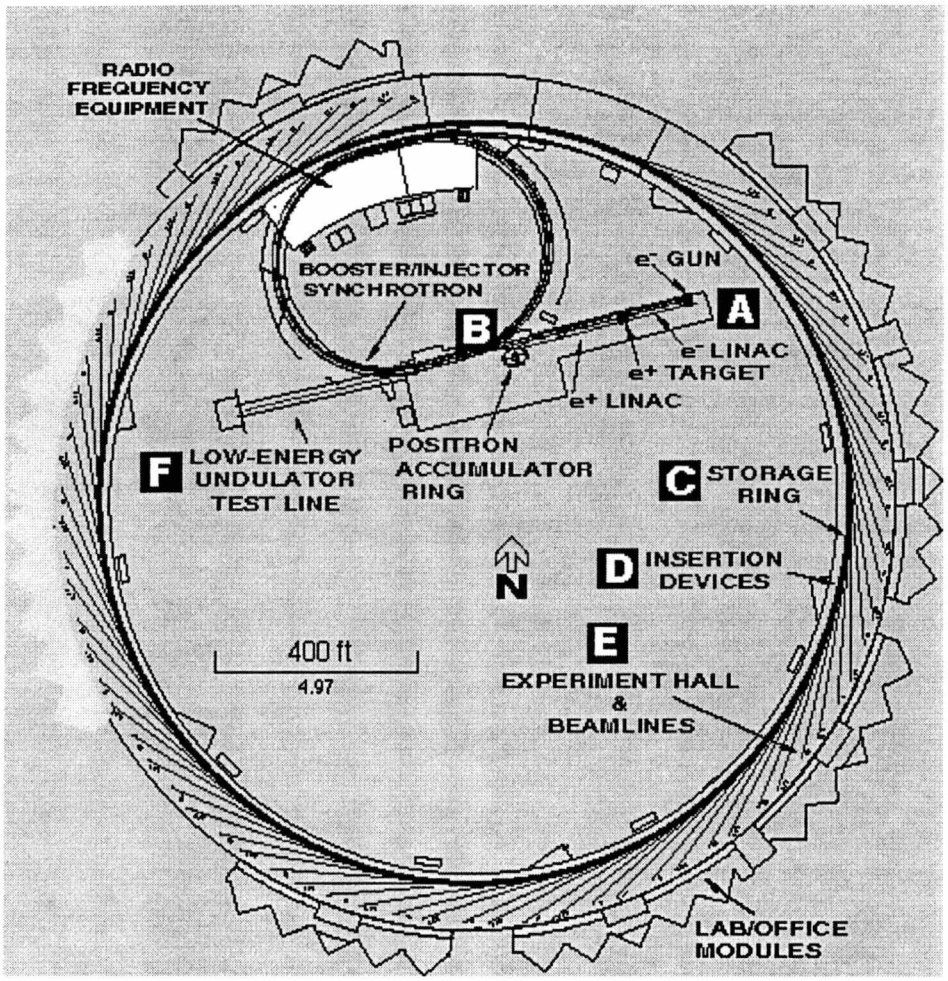

Figure A.1: Schematic diagram of the advanced photon source (APS)[1].

[1] The picture is taken from the APS Web site (http://www.aps.anl.gov)

(1) Continuous spectrum from infrared to the x-ray region.

(2) High intensity , collimation and coherence (a measure of electric vector phase relationship between photons).

(3) Linear and circular polarization.

(4) High spectral brilliance which refers to a focused beam with high intensity, narrow spectral distribution, and a small spot beam size.

(5) A time structure with pulse length down to 100 ps.

A.2 Beamline 2-ID at the Advanced Photon Source

Beamline 2-ID was used to perform the experiments of this thesis. The beam line is a dedicated insertion-device beamline which has been primarily designed for x-ray microfocusing and coherence-based techniques and applications.

Figure A.2 schematically shows the layout of major optical and vacuum components of the beamline 2-ID-D/E [25]. As can be seen in the figure, the front end of the beamline includes a standard undulator and a fixed –aperture. The undulator acts as the radiation source for the beamline and emits radiation at 4.4 kW. The fixed aperture located at 27.25 m from the center of insertion device (ID) reduces this power to 2.2 kW at a closed gap of 11.5 mm. It also has a 165 μrad angular acceptance for the synchrotron x-ray beam produced by the undulator A.

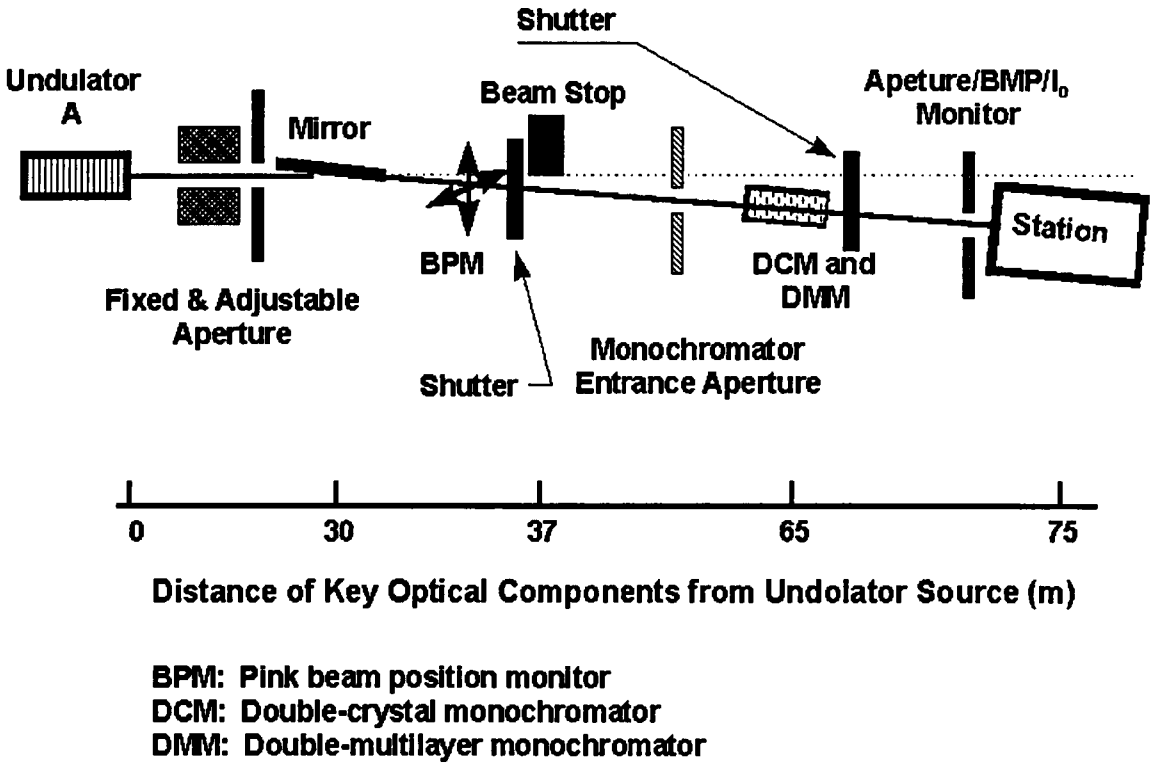

Figure A.2: Schematic diagram of beamline 2-ID at the advanced photon source (APS) [25].

The adjustable aperture is located at 28.25 m from the center of the ID and consists of two L-shaped knife blades that are water cooled. The main functions of this aperture are to reduce the beam size, to increase lateral coherence for coherence-based x-ray methods, and to improve spatial resolution for x-ray microfocusing techniques.

The horizontal mirror placed at 30 m from the ID source deflects the incident radiation toward the storage ring with a grazing angle of 0.15°. The mirror consists of three parallel bands of reflecting surfaces. These are a polished Si substrate and coated Pt and Rh layers. The major advantages of using such a mirror are: (1) substantial heat flux reduction for the downstream optical and nonoptical components, (2) considerable reduction in radiation shielding requirements, and (3) significant suppression of high order harmonics of the beamline radiation. In addition, the horizontal beam deflection by the mirror helps (1) preserve the source brilliance and the beam coherence in the vertical direction, (2) reduce slope errors induced by gravitational forces, and (3) maintain a standard beam height.

The two monochromators installed on the beamline are: (1) a symmetric double-crystal monochromator (DCM) and (2) a double-multilayer monochromator (DMM). The DCM located at 64 m from the source is used for experiments with high resolving power such as microspectroscopy, microdiffraction, and microimaging. The DMM located at 65 m from the source is used for applications with moderate resolving power such as micro-Laue diffraction and microfluorescence. The DCM is a novel Si 111 crystal which receives radiation with heat fluxes up to maximum 2.3 W/mm^2.

In the experiment station, the major x-ray instruments are a scanning x-ray microprobe and an imaging microscope. For the scanning microprobe, the focusing optic is either a phase zone plate or an elliptical mirror. The focusing optic may produce a focal spot as small as 0.1μm which is ideal for micro-inspection of advanced materials. The station is also equipped with a position–sensitive CCD detector and a 13-element Ge energy-dispersive detector. The CCD detector may be used for spatially resolved microdiffraction and imaging microscope applications and the Ge detector for x-ray fluorescence applications.

APPENDIX B

NUMERICAL AND COMPUTER IMPLEMENTATION OF BACK PROJECTION OF FILTERED PROJECTION

The numerical derivation of the filtered backprojection algorithm involves the application of both discrete Fourier transform and discrete inverse Fourier transform. The details of the derivation are well documented in references [20,21]. This appendix presents a brief summary of steps to show the numerical implementation of the filtered backprojection algorithm. Most information presented here is extracted form those references.

To start the numerical derivation of the filtered backprojection, we need to rewrite Equation (2.14) which is the integral form of the algorithm.

$$\mu(x,y) = \int_0^{\pi}\int_{-\infty}^{+\infty} P_F(\omega,\theta) e^{i\omega(x\cos\theta + y\sin\theta)} \mid \omega \mid g(\omega) d\theta d\omega \tag{B.1}$$

where $P_F(\omega,\theta)$ is the Fourier transform of the projection data.

$$P_F(\theta,\omega) = \int_{-\infty}^{+\infty}\int_{-\infty}^{+\infty} \mu(x,y) e^{-i\omega(x\cos\theta + y\sin\theta)} dxdy \quad = \int_{-\infty}^{+\infty} P(t,\theta) e^{-i\omega t} dt \tag{B.2}$$

Here $p(t,\theta)$ is the measured projection data. To ease the handling of Equation (B.1), the interior integral of the equation is denoted as

$$C(\theta,t) = \int_{-\infty}^{+\infty} P_F(\omega,\theta) e^{i\omega(x\cos\theta + y\sin\theta)} |\omega| g(\omega) d\omega \tag{B.3}$$

where $t = x\cos\theta + y\sin\theta$.

Now , Equation (B.1) can be written as

$$\mu(x,y) = \int_0^{\pi} C(\theta,t)d\theta \tag{B.4}$$

The above integral is numerically approximated as

$$\mu(x,y) \approx \frac{\pi}{q}\sum_{l=0}^{q-1} C(\theta_l,t) \tag{B.5}$$

where q is the number of projection angles and l is an index for the projection angle, for example, l = 0, 1, 2, ..., q-1.

To perform the numerical approximation of Equation (B.3) which determines $C(\theta_l,t)$, the following steps as described in Reference [20] are needed.

1. Add zeros to the projection data $p= (p_0, ..., p_{K-1})^T$ to form the new projection vector $p_n=(p_{-(K-1)}, ..., P_{K-1})^T$. This is required to avoid interperiod interferences resulting from the overlapping of the convolution result of one period over the that of succeeding period.

2. Take the discrete Fourier transform of p_n to obtain the frequency vector $P_{nF}(\omega,\theta)$.

3. Determine the frequency vector of a desired filter function ($|\omega|g(\omega)$) using of the filter functions described in Chapter 2. If a filter function is not already in the frequency domain, then take the discrete Fourier transform to determine the frequency vector of the filter. The length of filter vector is also from -(K-1) to K-1 (e.g;$b = b_{-(K-1)}, ..., b_{K-1}$).

4. Multiply $P_{nF}(\omega,\theta)$ by the filter function in the frequency domain and then take the discrete inverse Fourier transform of the result to determine $C(\theta_l,t)$.

Note that all the vectors, $P_{nF}(\omega,\theta)$, $|\omega|g(\omega)$, and $C(\theta_l,t)$ are length of 2K-1. The computer implementation of the above steps in Matlab environment is as follows.

$$C(\theta_l,t) = IDFT(DFT(p-(K-1):K-1)).*DFT(b(-(K-1):K-1))) \tag{B.6}$$

Here, DFT and IDFT refer to discrete Fourier and discrete inverse Fourier functions in Matlab software, respectively. The operation .* in Matlab stands for elementwise vector multiplication.

The following computer code in Matlab software demonstrates the implementation of backprojection of filtered projection algorithm for image reconstruction of an ellipse from a set of projection data. The projection data are calculated using the following equation derived from analytical methods [21].

$$P_\theta(t) = \frac{2\rho AB}{a^2(\theta)}\sqrt{a^2(\theta) - t^2} \qquad \text{for } |t| \le a(\theta)$$
$$= 0 \qquad \text{for } |t| > a(\theta) \qquad \text{(B.7)}$$

Where ρ is the object's density. The definitions of A, B, and a(θ) are given on Fig. B.1.

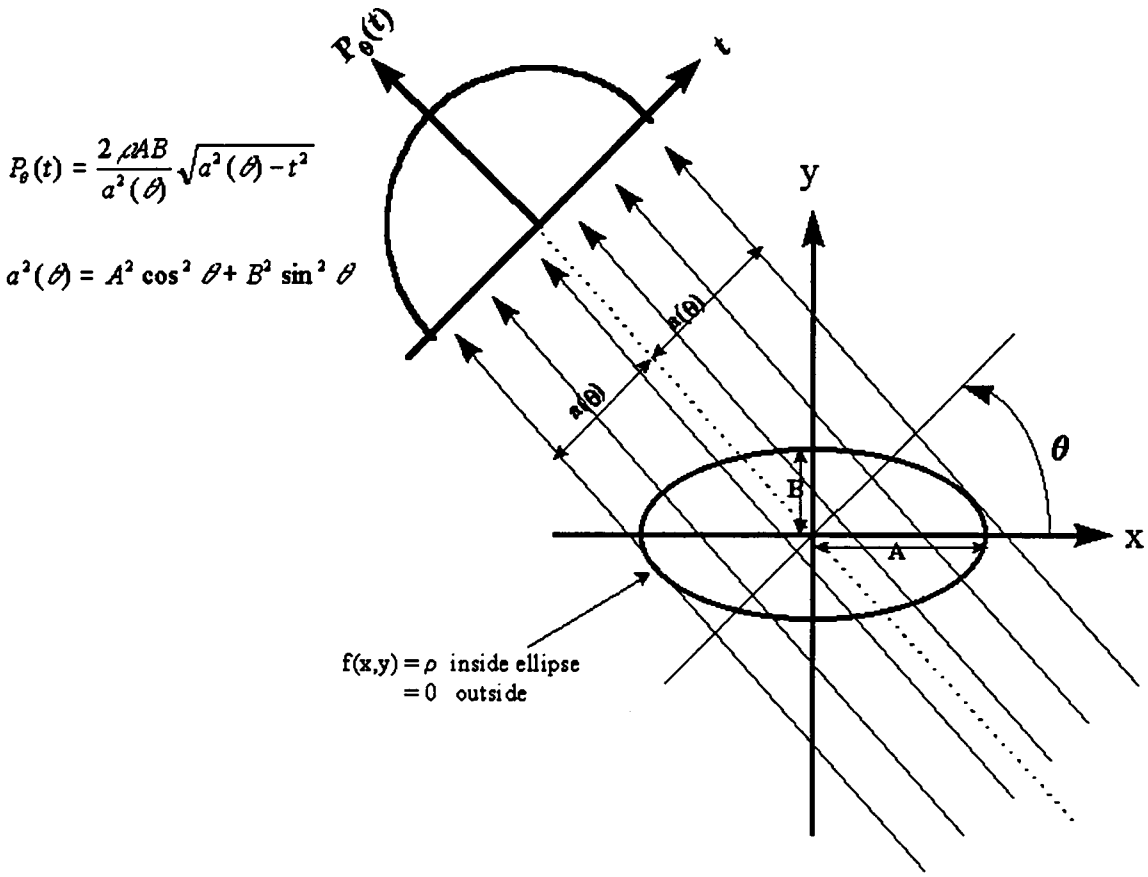

Figure B.1: Analytical projection data for an ellipse with a uniform density [21].

```
%*****************************************************************
%*                                                               *
%* This program first generates projection data for an ellipse of *
%* (X^2/A^2) + (Y^2/B^2) = 1 according to the Equation (B.7) of the thesis. *
%* Then, it uses the generated projection data in the backprojection of the *
%* filtered projections algorithm to reconstruct the ellipse. It is assumed *
%* that the ellipse has a uniform mass density.                  *
%*                                                               *
%* If the projection data is already available, then the first part of the *
%* program can be bypassed and the data can be directly used in the image *
%* reconstruction section of the program.                        *
%*                                                               *
%*            DEFINITION OF VARIABLES                            *
%*                                                               *
%* A:      (Major diameter of the ellipse)/2                     *
%* B:      (Minor diameter of the ellipse)/2                     *
%* ROH:    (Uniform mass density of the ellipse)                 *
%* NANG:   (Number of projection angles)                          *
%*                                                               *
%*****************************************************************
%*****************************************************************
%*          GENERATING PROJECTION DATA FOR THE ELLIPSE           *
%*****************************************************************
roh = 1;
A = input('Enter the major radius of the ellipse (A): ');
B = input('Enter the minor radius of the ellipse (B): ');
Nang = input('Enter the number of projection angles: ');
Step = input('Enter the number of sampling intervals (Dx): ');
increment1 = 180/Nang;
increment2 = (2*A)/Step;
n=0;
m=0;
angle=0;
for i = 0:Nang-1,

 n  = n+1;
 ir = increment1*i*(pi/180);
 at=sqrt( (A^2)*(cos(ir)^2)+(B^2)*(sin(ir)^2) );
 m=0;
 for j = 0:Step,

   t=-A+increment2*j;
   m=m+1;

   if abs(t) > at
    pt(n,m)=0;
```

```
  else
    pt(n,m) = ( (2*roh*A*B)/(at^2) )*(at^2 - t^2);
  end

 end

end

%*****************************************************************
%* IMAGE RECONSTRUCTION USING BACKPROJECTION OF FILTERED*
%* PROJECTION ALGORITHM                                          *
%*****************************************************************

for i = 1:n,

 for j = 1:m-1,
 pt1(i,j) =0;
 end

end

ptn =[pt,pt1];          % zero padding

%*****************************************************************
%*                    FILTER CALCULATIONS                        *
%*****************************************************************

ik=0;
for i=-(m-1):(m-1)
  ik=ik+1;
  if i==0
    b(ik)=1/(2*increment2)^2;
  elseif (rem(i,2)==0)
    b(ik)=0;
  else
    b(ik)=-1/(i*pi*increment2)^2;

  end
end

b1=[b(m+1:2*m-1), b(1:m)];


*****************************************************************
*                    FILTERED PROJECTIONS                       *
```

```
*****************************************************************

for k=1:n
C(k,1:2*m-1)=idft( dft(ptn(k,:)).*dft(b1) );
end


sum=0;
middle=Step/2;
x_mid=Step/2;
y_mid=Step/2;
fact1=1/(1.15*sqrt(2));

*****************************************************************
*              BACKPROJECTION OF FILTERED PROJECTIONS           *
*****************************************************************

for i=1:m
 for j=1:m

   for k=1:n
   angle=increment1*(k-1)*pi/180;
   t=cos(angle)*((i-x_mid)/(x_mid)) + sin(angle)*((j-y_mid)/(y_mid));
   midbin=middle*(t*fact1+1);
   f1=floor(midbin);
   f2=ceil(midbin);
   frac=midbin-f1;
    sum = sum + real(C(k,f1))*(1-frac) + real(C(k,f2))*frac;

   end
   u(i,j)=sum;
   sum=0;
 end
end
```

APPENDIX C

LISTING OF COMPUTER PROGRAMS

This appendix presents two computer codes used in this research. The first code processes the raw data collected by the data acquisition software in the APS and store them in two different files. File "Tomograf.dat" includes all the tomographic measurements without any normalization to the incident beam. This file is used in a commercial graphical package to obtain tomographic maps (sinograms) of each measured ROI. The second file, "Tomogarfn.dat", contains the normalized projection data used in the image reconstruction program. The structure of both files have been described in Chapter 4.

The second program is used to perform tomographic image reconstruction with and without absorption correction. The code employs numerous external image reconstruction subroutines from the library site RECLBL [19] to carry out the tomographic image reconstruction. The back-projection of the filtered projection and the Grady subroutines are used in this research. The normalized projection data are input to this program by an internal subroutine. Figure A.3 illustrates the image reconstruction grid for a parallel beam geometry and provides definitions for the image reconstruction parameters used in this program.

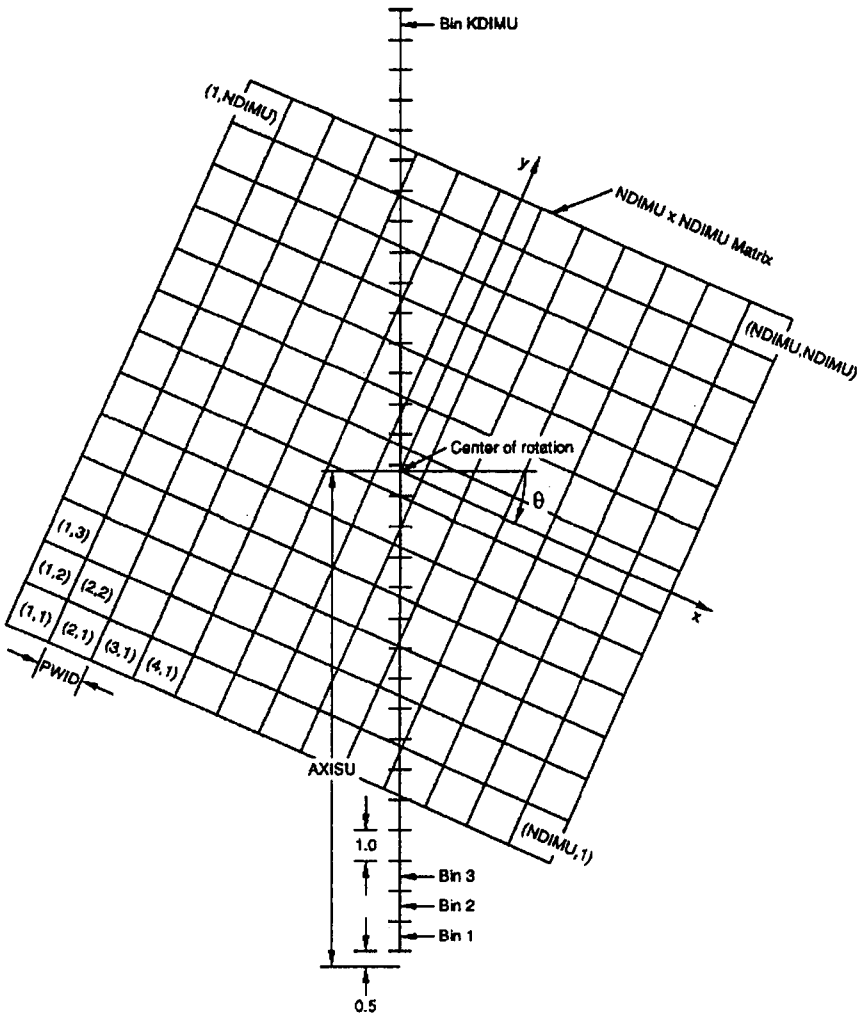

Figure C.1: Image reconstruction grid in a parallel-beam geometry [19].

```
************************************************************
*                                                          *
*  Program's Name:  Tomograf.for                           *
*                                                          *
*  This computer program processes tomographic projection data from  *
*  101 files and combine them into a single file by the name of      *
*  "Tomgraf.dat."The file Tomgraf.dat contains the raw data for 10 ROI,  *
*  Compton  and  elastic scattering, and MCA real time.  In addition, it  *
*  generates a second data file by the name of contains normalized   *
*  tomography data.  This file is used for  "ntomgrf.dat" which image  of  *
*  reconstruction routines. The structure the file is the same as that of  *
*  tomgraf.dat.                                                      *
*                                                                    *
*  The program also removes the unwanted data in the Kapton tape     *
*  and symmetrizes the data with respect to the center of rotation.  *
*  This reduces the data size from 101 to 94 data values for each    *
*  projection angle.                                                 *
*                                                                    *
*  The program also gives options to the user to smooth and          *
*  normalize data along the sinogram path of each ROI.               *
*                                                                    *
*  filename.txt:  Contains 101 filenames of tomography data          *
*  tomograf.dat:  Contains the combined data from 101 data files     *
*  ntomogr1.dat: Contains the normalized data from 101 files         *
*  ntomogrf.dat:  Contains the normalized and symmetrized data       *
*                 processed from 101 data files.                     *
*  atomogrf.dat:  Contains the smoothened, normalized, and           *
*                 symmetrized data processed from 101 data files.    *
*                                                                    *
************************************************************

      Real*4   pos(10300,2),flux1(10400,10),livetime(10300),
     &         flux0(10300),flux_av(10300),flux_av2(10000),
     &         flux2(10000,10),livetime2(10000),flux02(10000),
     &         pos2(10000,2),flux3(95,101,10)
      Character*35 file_na(110),dummy,choice,fname,ans


      Write(6,*)'Enter the the number of files to process: '
      Read(5,*) nfile
      Write(6,*)'Enter the number of unwanted lines (text lines)
     &        in the file's headerblock: '
      Read (5,*) n0
      Write(6,*)'Enter the number of columns in each data file: '
      Read (5,*) n1
        Write(6,*)'Do you want to remove the unwanted data from
```

```
&                Kapton tape?: '
      Read (5,*) choice
     Write(6,*)'Do you want to smooth the data'
      Read (5,*) ans
      fname='tomograf.dat'
      If (choice .eq. 'y') fname='aps1m.dat'

*************************************************************
*              INPUT/OUTPUT FILES                           *
*************************************************************

     Open (19, file='filename.txt',status='old')
     Open (21, file= fname,status='unknown')
     Open (22, file='ntomogr1.dat',status='unknown')
     Open (24, file='ntomogrf.dat',status='unknown')
     Open (25, file='atomogrf.dat',status='unknown')


     iflux =0

     Do nf=1,nfile          !OUTER LOOP getting the data files

     Read(19,*)file_na(nf)

     Open (20, file=file_na(nf),status='old')

     Do k=1,n0              !Bypassing the Headerblock
     Read(20,*)dummy
     End do

     Do while(.true.)    !LOOP for getting data from each data file

     i=i+1
     Read(20,*,end=12) pos(i,1),pos(i,2),flux0(i),(flux1(i,j),j=1,n1),
   &                   livetime(i)

     End do              !end do while

12    close(20)
     i=i-1
     end do              !END of the OUTER LOOP

       icount=i
       flux0(0)=flux0(1)
       flux0(icount+1)=flux0(icount)
```

```
      Do ii=1,icount

*****************************************************************
*          Smoothing out the Incident beam Flux (I0)            *
*****************************************************************

       flux_av(ii) =(flux0(ii-1)+flux0(ii)+flux0(ii+1))/3.0

*****************************************************************
*    Removing unwanted data from the Kapton Tape                *
*****************************************************************

    If (Choice .eq. 'y') then
    If((ii .ge.(1+irepeat)) .and. (ii .le. (9+irepeat))) then

      Do j=1,10
       flux1(ii,j)=0.0
      End do

      Endif

      If((ii .ge.(100+irepeat)) .and. (ii .le.(101+irepeat)))then

      Do j=1,10
       flux1(ii,j)=0.0
      End do

      Endif

      Endif          !END of Kapton Tape

*****************************************************************
*    Writing original data into data file, Tomogrfy.dat         *
*****************************************************************

    Write(21,11)pos(ii,2),iangle,(flux1(ii,j),j=1,n1),
  &             flux0(ii),flux_av(ii),livetime(ii)

*****************************************************************
*    Writing Normalized fluxes into data file, ntomogrf.dat.    *
*****************************************************************

      Write(22,10)pos(ii,2),iangle,(flux1(ii,j)/flux_av(ii),j=1,n1),
  &          flux0(ii),flux_av(ii),livetime(ii)
      irepeat=(ii/101)*101
    if ( (ii/101)*101 .eq. ii) iangle=iangle+3
```

```
      end do

*****************************************************************
*     Centering the data sets so that the center of the data    *
*     and the center of rotation coincide                       *
*****************************************************************

      ia =1
      Do i1 = 1,9494,94
      ik1=ik1+1
      if (i1 .ne. 1) ia=0

      Do i2= i1,94+i1-ia
      pos2(i2,2)=pos(i2+7*ik1,2)

      livetime2(i2)=livetime(i2+7*ik1)
      flux02(i2)=flux0(i2+7*ik1)
      flux_av2(i2)=flux_av(i2+7*ik1)

      Do j=1,10
      flux2(i2,j)=flux1(i2+7*ik1,j)
      End do

      End do


      End do
      If (ans .ne. 'y') GOTO 100


*****************************************************************
*     Smoothing of data in all ROIs along the Sinogram path     *
*     using only 5 data point.                                  *
*****************************************************************
C Rearranging the data so that they have a proper format for the
C Smoothing process.

      ik =0
      Do k=1,10      !Outer loop for ROIs

      Do j=1,101
      Do i=1,94

      ik=ik+1
      flux3(i,j,k)=flux2(ik,k)/flux_av2(ik)
```

```
      End do
      End do
      ik =0

      End do
      ik =0

*********************************************************************
* Smoothing of the data using 5 data points                         *
*********************************************************************

      Do k =1,10
      ik= 0

      Do j=1,101
      Do i=1,94

      ik=ik+1
      If (livetime2(ik) .GT. 2.6) then
      If((i .LT. 83).AND.(j .LT. 96))

     & flux3(i,j,k)=(flux3(i,j,k) +flux3(i+2,j+1,k)+ flux3(i+4,j+2,k)+
     & flux3(i+6,j+3,k)+flux3(i+8,j+4,k))/5.0

      If((i .GE. 83) .AND.(j .LT. 96))
     & flux3(i,j,k)=(flux3(i,j,k) +flux3(i-2,j+1,k)+ flux3(i-4,j+2,k)+
     & flux3(i-6,j+3,k)+flux3(i-8,j+4,k))/5.0
      End if

      If ((livetime2(ik) .GT. 4.0) .and. (i .le. 89) .and.(k .eq. 10))
     & flux3(i,j,10)=(flux3(i-1,j,10)+flux3(i+1,j,10))/2.0
      If ((livetime2(ik) .GT. 4.0) .and. (i .le. 89) .and.(k .eq. 9))
     & flux3(i,j,9)=(flux3(i,j,9)+flux3(i-1,j,9)+flux3(i+1,j,9))/3.0
      If ((livetime2(ik) .GT. 4.0) .and. (i .le. 89) .and.(k .eq. 8))
     & flux3(i,j,8)=(flux3(i,j,8)+flux3(i-1,j,8)+flux3(i+1,j,8))/3.0

      flux3(1,j,k)=0.0
      flux3(2,j,k)=0.0
      flux3(93,j,k)=0.0
      flux3(94,j,k)=0.0
      flux2(ik,k)=flux3(i,j,k)   !Returning the fluxes to the original format.

      End do
      End do
```

```
      End do
100  Continue
     iangle=0
     do ii =1,9494

     If(ans .ne. 'y') then
       Write(24,11)pos2(ii,2),iangle,(flux2(ii,j)/flux_av2(ii),j=1,n1),
    &                flux02(ii),flux_av2(ii),livetime2(ii)
     Else
        Write(25,10)pos2(ii,2),iangle,(flux2(ii,j),j=1,n1),
    &                flux02(ii),flux_av2(ii),livetime2(ii)
     End if

     If ( (ii/94)*94 .eq. ii) iangle=iangle+3

     End do


        Write(6,*)'Number of bad fluxes',iflux
        Close(22)

10     format(1x,f9.6,1x,I4,1x,14(2x,f14.7))
11     format(1x,f6.4,1x,I4,1x,14(1x,f14.7))


     End                        !End of program
```

IMAGE RECONSTRUCTION PROGRAM

```
*****************************************************************
*                                                               *
* PROGRAM:TOMOGRAPHIC IMAGE RECONSTRUCTION                      *
*                                                               *
* This program performs tomographic image reconstruction for a parallel  *
* beam geometry. The program employs image reconstruction routines from  *
* the library suite RECLBL to perform tomographic image reconstruction.  *
* Subroutine GETUM takes raw tomographic data and sends them to image    *
* reconstruction routines. The image reconstruction parameters are read  *
* from a data file by the name of "input.inf." This file is generated    *
* by the front-end of the code written in Visual Basic. The Visual       *
* Basic program provides a user friendly interface to interactively      *
* input data and information to the main program.                        *
*                                                                        *
* This program supports the following image reconstruction routines.     *
```

```
*                                                                    *
* 1. One dimensional convolution method with both RALA and SHLO      *
*    convolvers. The routine is called by Convo(X,XE,CNV,BCD,0)      *
*    where X is the reconstructed image, XE is the array of          *
*    uncertainties for X, CNV is the convolution subrotuine (RALA or *
*    SHLO), BCD is the back-projection subroutine using the concave  *
*    disk model, and the last term is the error flag set to be zero. *
*                                                                    *
* 2. Back-projection of filtered projections with HAN, HAM,BUTTERWORTH, *
*    PARZN, and RAMP filters. The routine is called byBKFIL(X,FIL,BCK, *
*    ORDERX, FREQX) where FIL is the filter subroutine, BCK is the back- *
*    projection subroutine, ORDERX is the filter parameter used only by *
*    the filter BUTTERWORTH, and FREQX is a filter parameter.        *
*                                                                    *
* 3. Minimizing Chi-square using the method of steepest descent. The *
*    routine is called by GRADY (X,PRJ,BCK,ISTP,IRLX,IERR,IZER) where *
*    PRJ and BCK are the projection and back-projection subroutines, *
*    ISTP is the number of iteration steps, IRLX is not equal to 0 for *
*    iterative relaxtion, IERR is not equal to 0 for weighted least- *
*    squares, and IZER is equal to 0 if intial solution equals 0. This *
*    routine is used for image reconstruction problems with constant *
*    absorption correction.                                          *
*                                                                    *
**********************************************************************


**********************************************************************
*                          M A I N   P R O G R A M                   *
**********************************************************************

      PROGRAM SiC_Shell

      IMPLICIT DOUBLE PRECISION (A-H,O-Z)
      DIMENSION X(30000),XE(30000),ag(180)
          integer achoice
          Character*50 fname1,fname2
      COMMON/BLANK/WORK(50000)

      COMMON/OUTCOM/LUNOUT,I80132
      COMMON/PARM/IPAR(12),PAR(4),NDP,Ichoice,ltype
      COMMON/Infile/fname1

**********************************************************************
*              IMAGE RECONSTRUCTION PARAMETERS                       *
**********************************************************************
```

```
      EQUIVALENCE (NDIMU ,IPAR( 1)),(ICIR  ,IPAR( 2)),(IGEOM ,IPAR( 3)),
     1        (NANG  ,IPAR( 4)),(MODANG,IPAR( 5)),(KDIMU ,IPAR( 6)),
     2        (IMIT  ,IPAR( 7)),(NWORK ,IPAR( 8)),(NFLOAT,IPAR( 9)),
     3        (ISTORE,IPAR(10)),(IPRINT,IPAR(11)),(LUNATN,IPAR(12)),
     4        (PWID  , PAR( 1)),(AXISU , PAR( 2)),(RFAN  , PAR( 3)),
     5        (CATN  , PAR( 4))

*******************************************************************
*          EXTERNAL SUBROUTINES CALLED FOR THE LIBRARY            *
*                    SUITE  RECLBL                                *
*******************************************************************

      EXTERNAL ham, brf, han, parzn, buter, ramp, bin, binf, shlo, laks, rala, bcd,
     &         prf, brfa, prfa

      LUNOUT=2
      I80132=0

*******************************************************************
*                GETTING INPUT DATA                               *
*******************************************************************

        Open(30,file='input.inf',status='old')

        Read(30,*)NDIMU      !Dimension of the reconstruction array

        Read(30,*)IGEOM      !A flag used to indicate the type of geometry
                             !IGEOM=0 is for parallel beam geometry.

        Read(30,*)NANG       !Number of projection angles.

        Read(30,*)MODANG     !is a mode flag for the input projection
                             !angles.  For MODANG=5 SETUP generates NANG
                             !projection angles equally spaced between 0
                             !and 2PI starting with 0.

        Read(30,*)KDIMU      !Dimension of the user's projection array.

        Read(30,*)IMIT       !A flag to indicate whether the reconstruction is
                             !of emission or transmission.
        Read(30,*)PWID       !The distance between neighboring reconstruction
                             !grid points relative to the projection bin width.

        Read(30,*)AXISU      !The location within the projection array where
                             !the rotation axis is projected.
```

```
      Read(30,*)ICIR      !An image reconstruction flag.

      Read(30,*)NDP       !Number of data points

      Read(30,*)Ltype     !Choice of filter

      Read(30,*)FREQX     !Filter parameter (cutoff frequency)

      Read(30,*)Orderx    !Order of filter

      Read(30,*)Ichoice   !A flag for choosing projection data of a
                          !desired ROI for image reconstruction.

      Read(30,*)fname1    !Filename for the projection data.

      Read(30,*)fname2    !Filename for the image reconstruction data

      Read(30,*)achoice   !A flag indicating whether absorption
                          !correction is needed or not

      Read(30,*)xlev      !Object to background ratio.

      Read(30,*)atenl     !A constant attenuation coefficient

      Read(30,*)Istp      !Number of iteration step in the GRADY
                          !routine

    NWORK=50000
    NFLOAT=2
    ISTORE=0
    IPRINT=12
    LUNATN=3
    RFAN =0.
    CATN =0.

    Factor3=1.4508e11   !number of SiC atoms in a pixel size of 1*1*3

*******************************************************************
*                    OUTPUT FILES                                 *
*******************************************************************


    Open (LUNOUT,FILE='Sic_bf.out',FORM='FORMATTED')
    Open (25,file='Sic_bf.dat',status='unknown')
    Open (26,file=fname2,status='unknown')
    Open (27,file='err.dat', status='unknown')
```

```
*****************************************************************
*          INVOKING IMAGE RECONSTRUCTION ROUTINES               *
*****************************************************************

      If (ltype .eq. 1)  call Convo(X,XE,SHLO,BCD,0)
      If (ltype .eq. 2)  call Convo(X,XE,RALA,BCD,0)
      If (ltype .eq. 3)  call BKFIL(X,HAN,BRF,ORDERX,FREQX)
      If (ltype .eq. 4)  call BKFIL(X,HAM,BRF,ORDERX,FREQX)
      If (ltype .eq. 5)  call BKFIL(X,PARZN,BRF,ORDERX,FREQX)
      If (ltype .eq. 6)  call BKFIL(X,BUTER,BRF,ORDERX,FREQX)
      If (ltype .eq. 7)  call BKFIL(X,RAMP,BRF,ORDERX,FREQX)
        if (achoice .eq. 1) then

        Open(lunout,file='e10.out',form='formatted')
        Open(lunatn,file='e10.tmp',form='unformatted',status='scratch')

        irlx=1
        ierr=0
        izer=0

        call Grady(x,prf,brf,istp,irlx,ierr,izer)

*****************************************************************
*  CALLING SUBROUTINE EVATU TO EVALUATE THE ATTENUATION
      *
*       FACTORS IN AN EMISSION SCAN USING A CONSTANT            *
*              ATTENUTION COEFFICIENT                           *
*****************************************************************

        call Evatu(x,xlev,atenl)
        irlx=1
        ierr=0
        izer=0

        Call grady(x,prfa,brfa,istp,irlx,ierr,izer)
        Endif

      Factor4 = 1000000./factor3

        if (Ichoice .eq. 12) factor4=1
      jk=0

*****************************************************************
*       REARRANGING THE OUTPUT DATA TO BE SUITABLE FOR          *
*              GRAPHICAL SOFTWARE PACKAGES                      *
```

```
*****************************************************************

      Do ik =1,NDIMU*NDIMU

         jk=jk+1
         If (x(ik) .lt. 0) x(ik)= 0.0
        Write(25,15)(jk-1)*8,iline*8,x(ik)*factor4
         If (jk .eq. ndimu) jk=0
         If ( (ik/ndimu)*ndimu .eq. ik) iline=iline+1
         If ((ltype .eq. 1) .or. (ltype .eq. 2)) write(27,15)(jk-1)*8,
  &                                iline*8,xe(ik)*factor4

      End do

       ik=0

      Do i=1,NDIMU

          Write(26,19)(x(kk),kk=1+ik,NDIMU+ik)
           ik =ik+NDIMU

      End do

      WRITE (LUNOUT,12)
      IF (IMIT.EQ.0) WRITE (LUNOUT,22)
      IF (IMIT.EQ.1) WRITE (LUNOUT,24)
      CALL ARRAY (X,NDIMU)



      CALL BCOM (MAXFW)

      CLOSE (LUNOUT)

 12  FORMAT(1X//' Reconstruction for Parallel Beam Geometry Uing Shl',
  1   'o Convolver')

 15 FORMAT(1x,I5,2x,I5,2x,F16.9)
 16 FORMAT(1X//' RECONSTRUCTION FOR PARALLEL BEAM GEOMETRY,
  1 USING RALA CONVOLVER')
 19 FORMAT(1x,201(f15.8,1x))
 22 FORMAT(' EMISSION DATA')
 24 FORMAT(' TRANSMISSION DATA')
   Write(6,*)'FINISHED'
   END
```

```
*****************************************************************
*****************************************************************
* THIS SUBROUTINE TAKES THE USER'S PROJECTION DATA AND          *
* SENDS THEM TO THE MAIN PROGRAM WITH A PROPER FORMAT.          *
* THE SUBROUTINE IS ADOPTED FROM THE RECLBL LIBRARY AND         *
* THEN MODIFIED TO BE SUITABLE FOR OUR PROBLEM.                 *
*                                                               *
*****************************************************************
*****************************************************************

      SUBROUTINE GETUM (M,DATA,ERR)

      IMPLICIT DOUBLE PRECISION (A-H,O-Z)

      DIMENSION DATA(*),ERR(*)
      Character*50 fname1

      COMMON/OUTCOM/LUNOUT,I80132
      COMMON/PARM/IPAR(12),PAR(4),NDP,Ichoice,ltype
      COMMON/Infile/fname1

      EQUIVALENCE (NDIMU ,IPAR( 1)),(ICIR  ,IPAR( 2)),(IGEOM ,IPAR( 3)),
     1        (NANG  ,IPAR( 4)),(MODANG,IPAR( 5)),(KDIMU ,IPAR( 6)),
     2        (IMIT  ,IPAR( 7)),(NWORK ,IPAR( 8)),(NFLOAT,IPAR( 9)),
     3        (ISTORE,IPAR(10)),(IPRINT,IPAR(11)),(LUNATN,IPAR(12)),
     4        (PWID  , PAR( 1)),(AXISU , PAR( 2)),(RFAN  , PAR( 3)),
     5        (CATN  , PAR( 4))


*****************************************************************
*         OPENNING THE PROJECTION DATA FILE ONLY ONCE           *
*                (ADDED TO THE SUBROUTINE)                      *
*****************************************************************

      If (ikk .eq. 0) Then

        Open(22, file=fname1, status='old')
        Open(23, file='check.dat',  status='unknown')

      End if

        isc = isc +1

      If (isc .gt. nang) then
```

```
      Rewind 22
        isc=0

    Endif

*****************************************************************
*          GETTING THE DESIRED ROI PROJECTION DATA FROM         *
*           THE DATA FILE (ADDED TO THE SUBROUTINE)             *
*****************************************************************

    Do i =1,NDP

    If (Ichoice .eq. 1) read(22,*)data(i)
        If (Ichoice .eq. 2) read(22,*)du1,data(i)
        If (Ichoice .eq. 3) read(22,*)du1,du2,data(i)
        If (Ichoice .eq. 4) read(22,*)du1,du2,du3,data(i)
        If (Ichoice .eq. 5) read(22,*)du1,du2,du3,du4,data(i)
        If (Ichoice .eq. 6) read(22,*)du1,du2,du3,du4,du5,data(i)
        If (Ichoice .eq. 7) read(22,*)du1,du2,du3,du4,du5,du6,data(i)
        If (Ichoice .eq. 8) read(22,*)du1,du2,du3,du4,du5,du6,du7,data(i)
        If (Ichoice .eq. 9) read(22,*)du1,du2,du3,du4,du5,du6,du7,du8,
   &    data(i)
        If (Ichoice .eq. 10) read(22,*)du1,du2,du3,du4,du5,du6,du7,du8,
   &    du9, data(i)
        If (Ichoice .eq. 11) read(22,*)du1,du2,du3,du4,du5,du6,du7,du8,
   &    du9,du10, data(i)
        If (Ichoice .eq. 12) read(22,*)du1,du2,du3,du4,du5,du6,du7,du8,
   &    du9,du10,du11, data(i)
         Write(23,*)i,data(i)



*****************************************************************
*        ESTIMATION OF UNCERTAINTIES IN THE PROJECTION DATA
       *
*          FOR THE CASE OF IMAGE RECONSTRUCTION WITH            *
*          CONVOLUTION METHOD (ADDED TO THE SUBROUTINE)         *
*****************************************************************

    If ((imit .eq. 0) .and. ((ltype .eq. 1) .or. (ltype .eq. 2)))Then


        dk=1.
        dk=max(data(i),dk)
```

```
    err(i)=sqrt(dk)
    Elseif ((imit .ne.0).and.((ltype .eq. 1).or.(ltype .eq. 2)))Then

    err(i)=1.
    end if

End do

ikk=ikk+1

RETURN
END
```

VITA

Masoud Naghedolfeizi was born in Tehran, Iran in 1961. He received his Bachelor of Science degree in Mechanical Engineering from Iran Science and Technology University in 1986. In August 1988, he entered the University of Tennessee to purse his graduate studies in the field of nuclear engineering. He received both his M.S. and Ph.D. degrees in Nuclear Engineering in December 1990 and 1994, respectively. His strong interest in the field of materials sciences encouraged him to pursue graduate studies in metallurgical engineering at the Department of Materials Science and Engineering of the University of Tennessee on part-time basis. He received the Master of Science degree in Metallurgical Engineering in December 1998. His research interests include x-ray tomography, reliability engineering with emphasis on life prediction technology, signal processing, and artificial intelligence. He is currently working at the position of assistant professor at the Fort Valley State University.